Comput. Methods Appl. Mech. Engrg. 199 (2010) 3250–3269

Contents lists available at ScienceDirect

Comput. Methods Appl. Mech. Engrg.

journal homepage: www.elsevier.com/locate/cma

Simulation of coupled microscale multiphysical-fields in particulate-doped dielectrics with staggered adaptive FDTD

T.I. Zohdi *

Department of Mechanical Engineering, 6195 Etcheverry Hall, University of California, Berkeley, CA 94720-1740, USA

ARTICLE INFO

Article history:
Received 24 March 2010
Received in revised form 22 June 2010
Accepted 25 June 2010
Available online 17 August 2010

Keywords:
Multiphysics
Material response
Heterogeneous materials

ABSTRACT

This work addresses the modeling and simulation of strongly coupled electromagnetic and thermodynamic fields that arise in particulate-doped dielectrics using an adaptive staggered adaptive FDTD (finite difference time domain) method. Of particular interest is to provide a straightforward modular approach to finding the effective dielectric (electromagnetic) response of a material, incorporating thermal effects, arising from Joule heating, which alter the pointwise dielectric properties such as the electric permittivity, magnetic permeability, and electric conductivity. This is important for "thermal (damage) management" of materials used in electromagnetic applications. Because multiple field coupling is present, a staggered, temporally-adaptive scheme is developed to resolve the internal microstructural electric, magnetic and thermal fields, accounting for the simultaneous pointwise changes in the material properties. Numerical examples are provided to illustrate the approach. Extensions to coupled chemical and mechanical fields are also provided.

1. Introduction

1.1. Effective properties

A variety of modern electromagnetic devices employ "new" materials, comprised of particulate-doped microstructure (Fig. 1). The particulates are chosen for their dielectric properties, in order to modify and enhance the dielectric properties of an easily formable matrix material. The overall permittivity of such materials is defined by

$$\langle \boldsymbol{D} \rangle_{\Omega} = \boldsymbol{\epsilon}^{*} \cdot \langle \boldsymbol{E} \rangle_{\Omega}, \tag{1.1}$$

where $\langle \cdot \rangle_{\Omega} \stackrel{\text{def}}{=} frac1|\Omega| \int_{\Omega} \cdot d\Omega$, is the averaging operator and $\boldsymbol{D}$ and $\boldsymbol{E}$ are the electric flux and electric field vectors within a statistically representative volume element (RVE) of volume $|\Omega|$. The quantity $\boldsymbol{\epsilon}^{*}$ is the effective permittivity tensor. Similarly, one can introduce effective magnetic properties such as

$$\langle \boldsymbol{B} \rangle_{\Omega} = \boldsymbol{\mu}^{*} \cdot \langle \boldsymbol{H} \rangle_{\Omega}, \tag{1.2}$$

where $\boldsymbol{B}$ and $\boldsymbol{H}$ are the magnetic flux and magnetic field vectors, and $\boldsymbol{\mu}^{*}$ is the effective magnetic permeability.

1.2. Estimates for effective dielectric responses

There are a variety of estimates for effective dielectric constants. The simplest estimates are the so-called Wiener bounds [44] (1910), $\langle \boldsymbol{\epsilon}^{-1} \rangle_{\Omega}^{-1} \leqslant \boldsymbol{\epsilon}^{*} \leqslant \langle \boldsymbol{\epsilon} \rangle_{\Omega}$, where the upper bound is generated by assuming that the electric field is uniform throughout the medium (within a suitable material sample) and the lower bound is generated by assuming that the electric field flux is uniform throughout the medium. These inequalities mean that the eigenvalues of the tensors $\boldsymbol{\epsilon}^{*} - \langle \boldsymbol{\epsilon}^{-1} \rangle_{\Omega}^{-1}$ and $\langle \boldsymbol{\epsilon} \rangle_{\Omega} - \boldsymbol{\epsilon}^{*}$ are non-negative. Similar results hold for the magnetic field ($\langle \boldsymbol{\mu}^{-1} \rangle_{\Omega}^{-1} \leqslant \boldsymbol{\mu}^{*} \leqslant \langle \boldsymbol{\mu} \rangle_{\Omega}$).

In the case of isotropic materials ($\boldsymbol{\epsilon} = \epsilon \mathbf{1}$ and $\boldsymbol{\mu} = \mu \mathbf{1}$), improved bounds were developed in 1962 by Hashin and Shtrikman [17] based on variational principles using the concept of polarization tensor fields (filtering/separation of micro–macro scales). Based on these formulations, they developed sharper bounds for the effective properties. The bounds are as follows, for the overall electrical permittivity

$$\langle \epsilon^{-1} \rangle_{\Omega}^{-1} \leqslant \underbrace{\epsilon_1 + \frac{v_2^{\epsilon}}{\frac{1}{\epsilon_2 - \epsilon_1} + \frac{1 - v_2^{\epsilon}}{3\epsilon_1}}}_{\stackrel{\text{def}}{=} \epsilon^{*,-}} \leqslant \epsilon^{*} \leqslant \underbrace{\epsilon_2 + \frac{1 - v_2^{\epsilon}}{\frac{1}{\epsilon_1 - \epsilon_2} + \frac{v_2^{\epsilon}}{3\epsilon_2}}}_{\stackrel{\text{def}}{=} \epsilon^{*,+}} \leqslant \langle \epsilon \rangle_{\Omega} \tag{1.3}$$

and the overall magnetic permeability

$$\langle \mu^{-1} \rangle_{\Omega}^{-1} \leqslant \underbrace{\mu_1 + \frac{v_2^{\mu}}{\frac{1}{\mu_2 - \mu_1} + \frac{1 - v_2^{\mu}}{3\mu_1}}}_{\stackrel{\text{def}}{=} \mu^{*,-}} \leqslant \mu^{*} \leqslant \underbrace{\mu_2 + \frac{1 - v_2^{\mu}}{\frac{1}{\mu_1 - \mu_2} + \frac{v_2^{\mu}}{3\mu_2}}}_{\mu^{*,+}} \leqslant \langle \mu \rangle_{\Omega}, \tag{1.4}$$

where $\epsilon_2 \geqslant \epsilon_1$, $\mu_2 \geqslant \mu_1$, v_2^{ϵ} is the volume fraction of phase with the larger ϵ value ("phase 2" in the former expression) for the

* Tel.: +1 510 642 9172; fax: +1 510 642 6163.
E-mail address: zohdi@me.berkeley.edu

0045-7825/$ - see front matter © 2010 Elsevier B.V. All rights reserved.
doi:10.1016/j.cma.2010.06.032

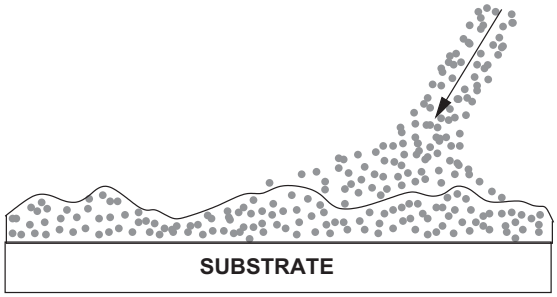

Fig. 1. Tailored dielectric materials constructed from dispersing particles within a binding matrix.

permittivity-mismatch and v_2^{μ} is the volume fraction of the phase with the larger μ value ("phase 2" in the latter expression) for the permeability-mismatch.[1] The Hashin–Shtrikman bounds are the sharpest possible bounds for isotropic effective responses, with isotropic two phase microstructures, where the only known information are the volume fractions and phase contrasts of the constituents. Note that no additional geometric information, such as the number and nature of particles, contributes to these bounds. These bounds and other analytical estimates are derived under the idealized conditions, such as electro- and magneto-statics (which decouples Maxwell's equations), non-conducting, loss-less media, thermal-insensitivity, etc., leading to a simplification that yield tractable to analytical solutions.[2]

Remark. Estimates for the effective properties of heterogeneous materials date back over 150 years to Maxwell [28,29] and Lord Rayleigh [36]. For a relatively recent and thorough analysis of a variety of classical approaches, such as the ones briefly mentioned here, see Torquato [40] for general interdisciplinary discussions, Jikov et al. [19] for more mathematical aspects, Aboudi [1], Hashin and Shtrikman [14,15,17], Hashin [16], Mura [30], Nemat-Nasser and Hori [31] for solid-mechanics inclined accounts of the subject and Zohdi and Wriggers [56] for computational aspects.

1.3. Thermal coupling

In general, the properties of most electromagnetic materials are quite sensitive to the temperature. For example, let us consider the three main electromagnetic properties, the electrical permittivity, magnetic permeability and electrical conductivity, in the isotropic case ($\boldsymbol{\epsilon} = \epsilon\mathbf{1}$, $\boldsymbol{\mu} = \mu\mathbf{1}$ and $\boldsymbol{\sigma} = \sigma\mathbf{1}$). Following common practice, for electromagnetic materials, we write $\epsilon = \epsilon_0\epsilon_r$ where $\epsilon_0 = 8.854 \times 10^{-12}$ farads/meter is the free space permittivity and ϵ_r is the relative permittivity or "dielectric" constant and $\mu_0 = 4\pi \times 10^{-7}\,\mathrm{Ns}^2/\mathrm{C}^2$ and $\mu = \mu_r\mu_0$, where μ_r is the relative magnetic permeability. As a "model problem" material, we consider the following decompositions, employing thermo-electromagnetic saturation conditions (Sigmoid functions, Fig. 2):

- For the electrical permittivity:

$$\begin{aligned}\epsilon(\theta,\boldsymbol{E}) &= \epsilon_o(1+\chi_E(\theta,\boldsymbol{E})) = \epsilon_o\epsilon_r(\theta,\boldsymbol{E})\\ &= \epsilon_o\epsilon_r(\theta_R,\boldsymbol{E}_R)\mathcal{E}(\theta-\theta_R,\boldsymbol{E}-\boldsymbol{E}_R),\end{aligned} \tag{1.5}$$

where χ_E is the electric susceptibility, θ is the temperature and the last term is a representation around a reference state, for example, using saturation-type Sigmoid functions of the form

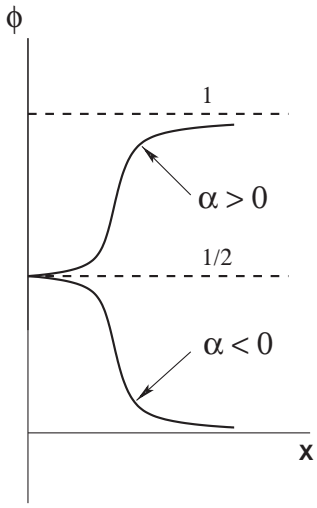

Fig. 2. General trends for Sigmoid-type behavior, where $\phi = (1+e^{-\alpha x})^{-1}$.

$$\begin{aligned}\mathcal{E}(\theta-\theta_R,\boldsymbol{E}-\boldsymbol{E}_R) = 1 &+ \mathcal{K}_{E1}\left(1+e^{-\alpha_{E1}(\theta-\theta_R)}\right)^{-1}\\ &+ \mathcal{K}_{E2}\left(1+e^{-\alpha_{E2}\|\boldsymbol{E}-\boldsymbol{E}_R\|}\right)^{-1},\end{aligned} \tag{1.6}$$

where the α's and $\mathcal{K}$'s are material parameters, and the terms with subscript "R" are reference values.

- For the magnetic permeability:

$$\begin{aligned}\mu(\theta,\boldsymbol{E}) &= \mu_o(1+\chi_H(\theta,\boldsymbol{H})) = \mu_o\mu_r(\theta,\boldsymbol{H})\\ &= \mu_o\mu_r(\theta_R,\boldsymbol{H}_R)\mathcal{H}(\theta-\theta_R,\boldsymbol{H}-\boldsymbol{H}_R),\end{aligned} \tag{1.7}$$

where χ_H is the magnetic susceptibility and, consistent with the pervious electrical decomposition

$$\begin{aligned}\mathcal{H}(\theta-\theta_R,\boldsymbol{H}-\boldsymbol{H}_R) = 1 &+ \mathcal{K}_{H1}\left(1+e^{-\alpha_{H1}(\theta-\theta_R)}\right)^{-1}\\ &+ \mathcal{K}_{H2}\left(1+e^{-\alpha_{H2}\|\boldsymbol{H}-\boldsymbol{H}_R\|}\right)^{-1}.\end{aligned} \tag{1.8}$$

- For the electrical conductivity:

$$\begin{aligned}\sigma(\theta,\boldsymbol{E}) = \sigma(\theta_R,\boldsymbol{E}_R)\Big(1 &+ \mathcal{K}_{S1}(1+e^{-\alpha_{S1}(\theta-\theta_R)})^{-1}\\ &+ \mathcal{K}_{S2}(1+e^{-\alpha_{S2}\|\boldsymbol{E}-\boldsymbol{E}_R\|})^{-1}\Big).\end{aligned} \tag{1.9}$$

Generally speaking, for many materials, until a saturation threshold is met, $\epsilon_r(\theta,\boldsymbol{E})$ grows with θ, $\mu_r(\theta,\boldsymbol{H})$ decreases with θ and $\sigma(\theta)$ decreases with θ. Because the electromagnetic field and subsequent flow of current through real materials leads to Joule heating, producing changes in the pointwise material properties, analytical predictions are somewhat limited, and one must resort to numerical schemes and so-called "mesoscale" computation, posed over a statistically representative volume element sample containing significant microstructure (several particles).

Remark. See the treatise of Jackson [18] for reviews of the rich variety of possible dielectrical responses of materials, including atomistic-level discussions to motivate non-linear dielectric behavior. Later, we shall utilize the previously mentioned specific "model-problem" decompositions (Eqs. (1.5)–(1.9)), however, the numerical formulations are developed for general cases.

1.4. Numerical methods

In order to properly capture the coupled (transient) electromagnetic and thermal behavior of a new material, Maxwell's equations, coupled to the First Law of Thermodynamics, must be solved (simultaneously) over a representative volume element. Thereaf-

[1] For either case, the volume fraction of the other phase is v_1, where $v_1 + v_2 = 1$.

[2] For example, electrostatics leads to a simplified version of Faraday's law, $\nabla_x \times \boldsymbol{E} = \boldsymbol{0}$ ($\boldsymbol{E}$ being the electric field), and Ampere's Law, $\nabla_x \times \boldsymbol{H} = \boldsymbol{0}$ ($\boldsymbol{H}$ being the magnetic field).

ter, the overall thermally-sensitive properties can be directly post-processed via volumetric averaging. The primary goal of this work is to develop numerical methods in order to ascertain the effects of particulates on the overall coupled response of thermally-sensitive dielectrics. There are a variety of computational electromagnetic methods (CEM) which can be lumped into two broad categories: differential equation formulations (DEF) and integral formulations (IF). In the DEF category, the most wide used techniques is the *finite difference time domain method* (FDTD), which is ideally suited to the problems of interest in this work. FDTD will serve as foundation of the approach developed in this work. However, in passing we mention other DEF-based methods, such as.

- *Multi resolution time domain method*: Solution techniques based on wavelet-based discretization,
- *Finite element method*: Solution techniques based on discretization of variational formulations and which are ideal for irregular geometries,[3]
- *Pseudo spectral time domain method*: Solution techniques based on Fourier and Chebyshev transforms, followed by a lattice or grid discretization of the transformed domain,

while in the IF category one has, for example,

- *Discrete dipole approximation*: Solution techniques based on an array of dipoles solved iteratively with the conjugate gradient method and a fast fourier transform to multiply matrices,
- *Method of moments*: Solution techniques based on integral formulations employing boundary element method discretization, often accompanied by the fast multipole method to accelerate summations needed during the calculations,
- *Partial element equivalent circuit method*: Solution techniques based on integral equations that are interpreted as circuits in discretization cells. This approach is ideal for circuit layout design.

The presentation is broken into three main parts: (1) formulations for each field, identifying the coupling terms, (2) iterative staggering schemes (including spatial and temporal discretization) and (3) numerical examples for model problems. Initially, we will focus on the electro–magneto–thermo fields, and then extend the formulations to include chemical and mechanical fields. The paper utilizes and extends low order (first order in space and time) FEM-based techniques originally developed in Zohdi [53,54] to simulate long-term diffusive systems modeling corrosion and to develop second-order (in both space and time) FDTD methods for electro–magneto–thermo–chemo–mechano type systems of interest to the electronics industry. The approach builds on work found in Zohdi [55], enlarging the types of fields in the system to include electro–magneto–thermo–chemo–mechano type systems, in addition to types of (semiconductor-like) constitutive laws for the electric permittivity, magnetic permeability and electrical conductivity, which are nonmonotone Sigmoid-type constitutive relations and providing a more in depth analysis of this type of system behavior. The developed approach is implicit, second-order accurate and relatively easy to encode. Unlike usual FDTD (explicit) methods, it is implicit, and is relatively robust, employing an adaptive staggering scheme to capture evolving multiphysics. This formulation is important for material designers who must seek ways by which to modify a base material, for example by employing particulate additives, however, simultaneously avoiding inadvertent overheating and thermal stresses.

[3] In particular, see Demkowicz et al. [7,8] and Rachowicz and Zdunek [35] for the state of the art in adaptive finite element methods for harmonic Maxwell's equations.

2. Transient electro–magneto–thermo coupled fields

We now provide the essential field equations that will be used during the mesoscale computation.

2.1. Electromagnetic fields: Maxwell's equations

In order to generate the overall (volume averaged) thermo-electromagnetic response of a heterogeneous continuum sample, we solve Maxwell's equations posed over a representative volume element (RVE) domain by starting with Faraday's Law

$$\nabla_x \times \boldsymbol{E} = -\left(\frac{\partial \boldsymbol{B}}{\partial t} + \boldsymbol{M}_s + \hat{\boldsymbol{\sigma}} \cdot \boldsymbol{H}\right) \tag{2.1}$$

and Ampere's Law

$$\nabla_x \times \boldsymbol{H} = \frac{\partial \boldsymbol{D}}{\partial t} + \boldsymbol{J}_s + \boldsymbol{\sigma} \cdot \boldsymbol{E}, \tag{2.2}$$

where we recall that $\boldsymbol{E}$ is the electric field, $\boldsymbol{D} = \boldsymbol{\epsilon} \cdot \boldsymbol{E}$ is the electric field flux, $\boldsymbol{J}_s$ is the source electric current, $\boldsymbol{H}$ is the magnetic field, $\boldsymbol{B} = \boldsymbol{\mu} \cdot \boldsymbol{H}$ is the magnetic field flux, $\boldsymbol{M}_s$ is the source "equivalent magnetic current", $\boldsymbol{\epsilon}$ is the electric permittivity, $\boldsymbol{\mu}$ is the magnetic permeability, $\boldsymbol{\sigma}$ is the electric conductivity and $\hat{\boldsymbol{\sigma}}$ is the equivalent magnetic loss. The material is assumed to be heterogeneous (spatially variable), isotropic, and thermally-sensitive.

Remark. $\boldsymbol{M}_s$ is a phenomenological term that frequently appears in the literature to account for magnetic "sources/losses" and "magnetic conduction". We shall keep these terms throughout the formulations, but with an implicit "warning" that they are difficult to justify from first principles. Furthermore, $\hat{\sigma}$ can be considered as the equivalent *phenomenological* magnetic "conductivity" (loss).

2.2. Thermodynamics: first law and absorption of energy

The interconversions of various forms of energy (electromagnetic, thermal, etc.) in a system are governed by the first law of thermodynamics,

$$\rho \dot{w} - \boldsymbol{T} : \nabla_x \dot{\boldsymbol{u}} + \nabla_x \cdot \boldsymbol{q} - \rho z = 0, \tag{2.3}$$

where w is the stored energy per unit mass (which is a function of the temperature, θ), ρ is the density, $\boldsymbol{T}$ is Cauchy stress, $\boldsymbol{u}$ is the displacement field, $\boldsymbol{q}$ is heat flux, and ρz is the rate of electromagnetic energy absorbed due to as Joule heating

$$\rho z = a(\boldsymbol{E} \cdot \boldsymbol{J}^{tot} + \boldsymbol{H} \cdot \boldsymbol{M}^{tot}), \tag{2.4}$$

where $0 \leqslant a \leqslant 1$ is an absorption constant, $\boldsymbol{J}^{tot} \stackrel{\text{def}}{=} \boldsymbol{J}_s + \boldsymbol{\sigma} \cdot \boldsymbol{E}$ and $\boldsymbol{M}^{tot} \stackrel{\text{def}}{=} \boldsymbol{M}_s + \hat{\boldsymbol{\sigma}} \cdot \boldsymbol{H}$. We consider the effects of deformation and stress to be insignificant in the present class of problems (the effects of stress are considered later), thus

$$\rho \dot{w} + \nabla_x \cdot \boldsymbol{q} - \rho z = 0 \tag{2.5}$$

and consider the stored thermal energy per unit mass to be $w = C\theta$ and Fourier's $\boldsymbol{q} = -\mathbb{K} \cdot \nabla_x \theta$. These assumptions lead to

$$\rho C \dot{\theta} - \nabla_x \cdot \mathbb{K} \cdot \nabla_x \theta - a(\boldsymbol{E} \cdot \boldsymbol{J}^{tot} + \boldsymbol{H} \cdot \boldsymbol{M}^{tot}) = 0, \tag{2.6}$$

where C is the heat capacity per unit mass and $\mathbb{K}$ is the thermal conductivity.

Remark 1. As mentioned in the introduction, we consider the pointwise properties, $\boldsymbol{\epsilon}(x)$, $\mu(x)$ and $\sigma(x)$ to be thermally-dependent, for example, governed by Eqs. (1.5)–(1.9).

Remark 2. Joule heating can be motivated by forming the inner product of the magnetic field with Faraday's law:

$$\boldsymbol{H}\cdot(\nabla_x\times\boldsymbol{E}) = -\boldsymbol{H}\cdot\left(\underbrace{\boldsymbol{M}_s+\hat{\sigma}\boldsymbol{H}}_{\boldsymbol{M}^{tot}}+\frac{\partial\boldsymbol{B}}{\partial t}\right) \tag{2.7}$$

and the inner product of the electric field with Ampere's law:

$$\boldsymbol{E}\cdot(\nabla_x\times\boldsymbol{H}) = \boldsymbol{E}\cdot\left(\underbrace{\boldsymbol{J}_s+\sigma\boldsymbol{E}}_{\stackrel{\text{def}}{=}\boldsymbol{J}^{tot}}+\frac{\partial\boldsymbol{D}}{\partial t}\right). \tag{2.8}$$

Subtracting Eq. (2.7) from Eq. (2.8) yields

$$\underbrace{\boldsymbol{E}\cdot(\nabla_x\times\boldsymbol{H})-\boldsymbol{H}\cdot(\nabla_x\times\boldsymbol{E})}_{-\nabla_x\cdot(\boldsymbol{E}\times\boldsymbol{H})=-\nabla_x\cdot\boldsymbol{S}} = \boldsymbol{E}\cdot\boldsymbol{J}^{tot}+\boldsymbol{H}\cdot\boldsymbol{M}^{tot}+\underbrace{\boldsymbol{E}\cdot\frac{\partial\boldsymbol{D}}{\partial t}+\boldsymbol{H}\cdot\frac{\partial\boldsymbol{B}}{\partial t}}_{=\frac{\partial W}{\partial t}}, \tag{2.9}$$

where $W=\frac{1}{2}(\boldsymbol{E}\cdot\boldsymbol{D}+\boldsymbol{H}\cdot\boldsymbol{B})=\frac{1}{2}(\boldsymbol{E}\cdot\boldsymbol{\epsilon}\cdot\boldsymbol{E}+\boldsymbol{H}\cdot\boldsymbol{\mu}\cdot\boldsymbol{H})$ is the electromagnetic energy and where $\boldsymbol{S}=\boldsymbol{E}\times\boldsymbol{H}$ is the Poynting vector. Thus

$$\frac{\partial W}{\partial t}+\nabla_x\cdot\boldsymbol{S} = -(\boldsymbol{E}\cdot\boldsymbol{J}^{tot}+\boldsymbol{H}\cdot\boldsymbol{M}^{tot}). \tag{2.10}$$

Eq. (2.10) is usually referred to as Poynting's theorem, and can be interpreted, *for simple material laws, where the previous representation for W holds*, as stating that the rate of change of electromagnetic energy within a volume, plus the energy flowing out through a boundary, is equal to the negative of the total work done by the fields on the sources and conduction. This work is then converted into thermo-mechanical energy. We consider the absorbed energy that is available for heating to be proportional to the energy associated with conduction, namely, from Eq. (2.10), $\boldsymbol{E}\cdot\boldsymbol{J}^{tot}+\boldsymbol{H}\cdot\boldsymbol{M}^{tot}$, and account for it via $\rho z = a(\boldsymbol{E}\cdot\boldsymbol{J}^{tot}+\boldsymbol{H}\cdot\boldsymbol{M}^{tot})$, where a is an absorption constant, $0\leqslant a\leqslant 1$. This type of simple model for heating is often referred to "Joule heating". On a smaller scale, one can interpret Joule heating as arising from charged particles being pulled through a medium by electromagnetic fields, which give up some of their kinetic energy when they collide with their surroundings, generating heat.

Remark 3. For illustration purposes, if one considers a one-dimensional steady-state problem (Fig. 3), ignoring the effects of stress, and assuming $\rho C\dot{\theta}=\rho C\dot{w}$

$$\rho C\dot{\theta} = 0 = K\frac{d^2\theta}{dx^2}+JE \Rightarrow \theta(x) = \theta(L)+\frac{JE}{2K}(L^2-x^2), \tag{2.11}$$

the maximum temperature becomes ($H=JE$, and assuming $J=\sigma E$ or $E=RJ$)

$$\theta(0)=\theta^{max}=\theta(L)+\underbrace{\frac{RJ^2}{2K}L^2}_{\text{thermal source}}, \tag{2.12}$$

which clearly shows the contribution of the Joule heating to the rise in temperature.

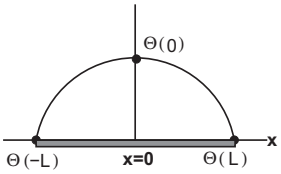

Fig. 3. A one-dimensional structure.

3. Numerical simulations: staggering schemes for thermo-electromagnetically coupled problems

We now develop a staggering solution framework to solve the coupled systems of interest. The general methodology is as follows (at at given time increment): (1) each field equation is solved individually, "freezing" the other (coupled) fields in the system, allowing only the primary field to be active and (2) after the solution of each field equation, the primary field variable is updated, and the next field equation is treated in a similar manner. For an "implicit" type of staggering, the process can be repeated in an iterative manner, while for an "explicit" type one moves to the next time step after one "pass" through the system. We will employ implicit staggering. Specifically, for the thermo–electro–magneto system under consideration, consider an abstract setting, whereby one solves for the electric field, assuming the magnetic and thermal fields are fixed (L is a time-step counter and K is a staggering-step counter),

$$\mathcal{A}_1\left(\underline{\boldsymbol{E}^{L+1,K}},\boldsymbol{H}^{L+1,K-1},\theta^{L+1,K-1}\right) = \mathcal{B}_1(\boldsymbol{E}^{L+1,K-1},\boldsymbol{H}^{L+1,K-1},\theta^{L+1,K-1}) \tag{3.1}$$

then one solves for the magnetic fields, assuming the electric and thermal fields fixed,

$$\mathcal{A}_2\left(\boldsymbol{E}^{L+1,K},\underline{\boldsymbol{H}^{L+1,K}},\theta^{L+1,K-1}\right) = \mathcal{B}_2(\boldsymbol{E}^{L+1,K},\boldsymbol{H}^{L+1,K-1},\theta^{L+1,K-1}) \tag{3.2}$$

then one solves for the thermal fields, assuming the electric and magnetic fields fixed,

$$\mathcal{A}_3\left(\boldsymbol{E}^{L+1,K},\boldsymbol{H}^{L+1,K},\underline{\theta^{L+1,K}}\right) = \mathcal{B}_3(\boldsymbol{E}^{L+1,K},\boldsymbol{H}^{L+1,K},\theta^{L+1,K-1}), \tag{3.3}$$

where the only underlined variable is "active" at that stage of the process. Within the staggering (iterative) scheme, implicit time-stepping methods (with time-step size adaptivity) will be used throughout the upcoming analysis (described shortly). The process is driven by minimizing the following normalized errors (for the three fields) within each time step, which represent the non-dimensional ratios for each field of the iterative error within a time-step (difference between successive iterations) to the difference in the converged solution from time-step to time-step; for the electric field[4]

$$\varpi_E^K \stackrel{\text{def}}{=} \frac{\|\boldsymbol{E}^{L+1,K}-\boldsymbol{E}^{L+1,K-1}\|}{\|\boldsymbol{E}^{L+1,K}-\boldsymbol{E}^{L}\|}, \tag{3.4}$$

for the magnetic field

$$\varpi_H^K \stackrel{\text{def}}{=} \frac{\|\boldsymbol{H}^{L+1,K}-\boldsymbol{H}^{L+1,K-1}\|}{\|\boldsymbol{H}^{L+1,K}-\boldsymbol{H}^{L}\|} \tag{3.5}$$

and for the thermodynamic field

$$\varpi_\theta^K \stackrel{\text{def}}{=} \frac{\|\theta^{L+1,K}-\theta^{L+1,K-1}\|}{\|\theta^{L+1,K}-\theta^{L}\|}. \tag{3.6}$$

Thereafter, we select the maximum *non-dimensionalized* error for adaptivity

$$\varpi^{*,K} \stackrel{\text{def}}{=} max(\varpi_E^K,\varpi_H^K,\varpi_\theta^K) \tag{3.7}$$

and determine whether the iterations should continue, or the time steps should be adaptively reduced (or increased if convergence occurs too quickly). The details of this process are discussed shortly. Generally speaking, if a recursive staggering process is not employed (an explicit coupling scheme), the staggering error can accumulate rapidly. However, simply employing extremely small time steps, smaller than needed to control the discretization error, in order to suppress a (nonrecursive) staggering process error, can be

[4] The symbol $\|\cdot\|$ will signify the $L^2(\Omega)$-norm throughout this work.

computationally inefficient. Therefore, the objective of the next subsection is to develop a strategy to adaptively adjust, in fact maximize, the choice of the time-step size in order to control the staggering error, while simultaneously staying below a critical time-step size needed to control the discretization error. An important related issue is to simultaneously minimize the computational effort involved. We now develop a staggering scheme by extending an approach found in the work of Zohdi et al. [53–56].

Remark. Staggering schemes are widely used in the computational mechanics literature, dating back, at least, to Zienkiewicz [47] and Zienkiewicz et al. [48]. For in depth overviews, see the works of Lewis and Schrefler (Lewis et al. [23] and Lewis and Schrefler [24]) and a series of works by Schrefler and collaborators: Schrefler [37], Turska and Schrefler [41], Biano et al. [5] and Wang and Schrefler [42].

3.1. Spatial discretization of the coupled system

3.1.1. Spatial discretization of the electromagnetic field

Numerically, the components of the curl of functions such as $\boldsymbol{E}$ and $\boldsymbol{H}$ are approximated by central finite difference stencils of the form (Fig. 4):

$$\left.\frac{\partial \boldsymbol{E}}{\partial x}\right|_x \approx \frac{\boldsymbol{E}(x+\Delta x)-\boldsymbol{E}(x-\Delta x)}{2\Delta x} \quad \text{and} \quad \left.\frac{\partial \boldsymbol{H}}{\partial x}\right|_x \approx \frac{\boldsymbol{H}(x+\Delta x)-\boldsymbol{H}(x-\Delta x)}{2\Delta x}, \tag{3.8}$$

for each of the (x_1, x_2, x_3)-directions, in order to form the terms needed in $\nabla_x \times \boldsymbol{E}$ and $\nabla_x \times \boldsymbol{H}$. This is a second-order accurate stencil. To illustrate this, consider a Taylor series expansion for an arbitrary function A

$$A(x+\Delta x) = A(x) + \left.\frac{\partial A}{\partial x}\right|_x \Delta x + \frac{1}{2}\left.\frac{\partial^2 A}{\partial x^2}\right|_x (\Delta x)^2 + \frac{1}{6}\left.\frac{\partial^3 A}{\partial x^3}\right|_x (\Delta x)^3 + \mathcal{O}(\Delta x)^4 \tag{3.9}$$

and

$$A(x-\Delta x) = A(x) - \left.\frac{\partial A}{\partial x}\right|_x \Delta x + \frac{1}{2}\left.\frac{\partial^2 A}{\partial x^2}\right|_x (\Delta x)^2 - \frac{1}{6}\left.\frac{\partial^3 A}{\partial x^3}\right|_x (\Delta x)^3 + \mathcal{O}(\Delta x)^4. \tag{3.10}$$

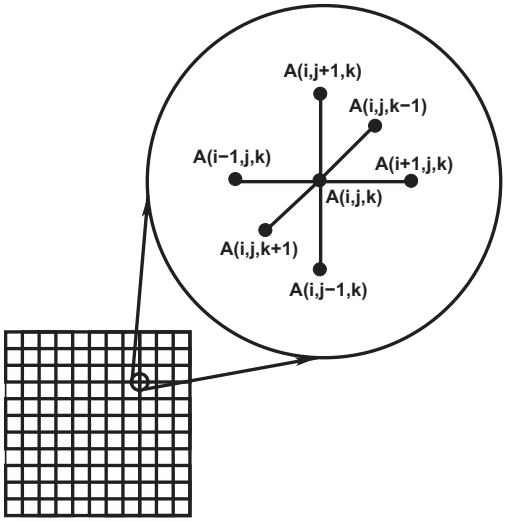

Fig. 4. A typical three dimensional finite difference stencil for a field $A(x, y, z)$.

Subtracting the two expressions yields

$$\left.\frac{\partial A}{\partial x}\right|_x = \frac{A(x+\Delta x)-A(x-\Delta x)}{2\Delta x} + \mathcal{O}(\Delta x)^2. \tag{3.11}$$

3.1.2. Spatial discretization of the thermal field

Although the discretization of the thermal field follows the same approach as the electromagnetic field, because it is governed by a second-order differential equation, the following approximation is first made

$$\left.\frac{\partial q}{\partial x}\right|_x \approx \frac{q\left(x+\frac{\Delta x}{2}\right)-q\left(x-\frac{\Delta x}{2}\right)}{\Delta x}, \tag{3.12}$$

where (in conjunction with Fourier's Law)

$$q\left(x+\frac{\Delta x}{2}\right) \approx -\mathbb{K}\left(x+\frac{\Delta x}{2}\right)\underbrace{\frac{\theta(x+\Delta x)-\theta(x)}{\Delta x}}_{\left.\frac{\partial \theta}{\partial x}\right|_{x+\frac{\Delta x}{2}}} \tag{3.13}$$

and

$$q\left(x-\frac{\Delta x}{2}\right) \approx -\mathbb{K}\left(x+\frac{\Delta x}{2}\right)\underbrace{\frac{\theta(x)-\theta(x-\Delta x)}{\Delta x}}_{\left.\frac{\partial \theta}{\partial x}\right|_{x-\frac{\Delta x}{2}}}, \tag{3.14}$$

where

$$\mathbb{K}\left(x+\frac{\Delta x}{2}\right) \approx \frac{1}{2}(\mathbb{K}(x+\Delta x)+\mathbb{K}(x)) \tag{3.15}$$

and

$$\mathbb{K}\left(x-\frac{\Delta x}{2}\right) \approx \frac{1}{2}(\mathbb{K}(x)+\mathbb{K}(x-\Delta x)). \tag{3.16}$$

These approximations are made for $\frac{\partial q_1}{\partial x_1}, \frac{\partial q_2}{\partial x_2}$ and $\frac{\partial q_3}{\partial x_3}$, in order to form the terms needed in $\nabla_x \cdot \boldsymbol{q}$.

3.2. Temporal discretization of the coupled system

3.2.1. Temporal discretization of the electromagnetic fields

We start with a relatively ("lossy") formulation of Maxwell's equations (Faraday's law and Ampere's law)

$$\frac{\partial(\boldsymbol{\mu}\cdot\boldsymbol{H})}{\partial t} = -\nabla_x \times \boldsymbol{E} - \boldsymbol{M}_s - \hat{\boldsymbol{\sigma}}\cdot\boldsymbol{H} \stackrel{\text{def}}{=} \boldsymbol{F} \tag{3.17}$$

and

$$\frac{\partial(\boldsymbol{\epsilon}\cdot\boldsymbol{E})}{\partial t} = \nabla_x \times \boldsymbol{H} - \boldsymbol{J}_s - \boldsymbol{\sigma}\cdot\boldsymbol{E} \stackrel{\text{def}}{=} \boldsymbol{G}. \tag{3.18}$$

We discretize for time = $t + \phi\Delta t$, and using a trapezoidal "ϕ-scheme" ($0 \leqslant \phi \leqslant 1$, see Appendix)

$$\frac{(\boldsymbol{\mu}\cdot\boldsymbol{H})(t+\Delta t)-(\boldsymbol{\mu}\cdot\boldsymbol{H})(t)}{\Delta t} \approx \boldsymbol{F}(t+\phi\Delta t) \approx \phi\boldsymbol{F}(t+\Delta t)+(1-\phi)\boldsymbol{F}(t) \tag{3.19}$$

and

$$\frac{(\boldsymbol{\epsilon}\cdot\boldsymbol{E})(t+\Delta t)-(\boldsymbol{\epsilon}\cdot\boldsymbol{E})(t)}{\Delta t} \approx \boldsymbol{G}(t+\phi\Delta t) \approx \phi\boldsymbol{G}(t+\Delta t)+(1-\phi)\boldsymbol{G}(t). \tag{3.20}$$

Rearranging, yields

$$\boldsymbol{H}(t+\Delta t) \approx \boldsymbol{\mu}^{-1}(t+\Delta t)\cdot((\boldsymbol{\mu}\cdot\boldsymbol{H})(t)+\Delta t(\phi\boldsymbol{F}(t+\Delta t)+(1-\phi)\boldsymbol{F}(t))) \tag{3.21}$$

and

$$\boldsymbol{E}(t+\Delta t) \approx \boldsymbol{\epsilon}^{-1}(t+\Delta t)\cdot((\boldsymbol{\epsilon}\cdot\boldsymbol{E})(t)+\Delta t(\phi\boldsymbol{G}(t+\Delta t)+(1-\phi)\boldsymbol{G}(t))), \tag{3.22}$$

where the previously introduced spatial discretization is applied to the terms in $\boldsymbol{F}$ and $\boldsymbol{G}$ ($\nabla_x \times \boldsymbol{H}$ and $\nabla_x \times \boldsymbol{E}$). Clearly, other constitutive laws, for example for the conduction, $\boldsymbol{J} = \mathcal{J}(\boldsymbol{E})$ can easily be handled with the same formulation. Note that the non-linearity can be far more complicated, and not easily separable, and one must resort to using a Taylor series expansion of the form

$$\boldsymbol{D}^K = \mathscr{f}(\boldsymbol{E}^K) \approx \mathscr{f}(\boldsymbol{E}^{K-1}) + \left.\frac{\partial \mathscr{f}}{\partial \boldsymbol{E}}\right|_{\boldsymbol{E}^{K-1}} \cdot (\boldsymbol{E}^K - \boldsymbol{E}^{K-1}) + \cdots + \mathcal{O}(\boldsymbol{E})^2 \tag{3.23}$$

and

$$\boldsymbol{B}^K = \mathscr{g}(\boldsymbol{H}^K) \approx \mathscr{g}(\boldsymbol{H}^{K-1}) + \left.\frac{\partial \mathscr{g}}{\partial \boldsymbol{H}}\right|_{\boldsymbol{H}^{K-1}} \cdot (\boldsymbol{H}^K - \boldsymbol{H}^{K-1}) + \cdots + \mathcal{O}(\boldsymbol{H})^2, \tag{3.24}$$

to linearize the system. Depending on the type of non-linearity, there may be slight advantages in arranging the fixed-point iteration in a certain order over another.

Remark. When $\phi = 1$, then this approach can be considered to be a (implicit) Backward Euler scheme, which is very stable (very dissipative) and $\mathcal{O}(\Delta t)^2$ locally in time, while if $\phi = 0$, the scheme can be considered as a (explicit) Forward Euler scheme, which is conditionally stable and $\mathcal{O}(\Delta t)^2$ locally in time and if $\phi = 0.5$, then the scheme can be considered as a (implicit) Midpoint scheme, which is marginally stable and $\widehat{\mathcal{O}}(\Delta t)^2 = \mathcal{O}(\Delta t)^3$ locally in time.

3.2.2. Temporal discretization of the thermal field

For the thermal field we write

$$\frac{\partial \theta}{\partial t} = \frac{1}{\rho C}(-\nabla_x \cdot \boldsymbol{q} + \rho z) \stackrel{\text{def}}{=} \boldsymbol{Y}. \tag{3.25}$$

We discretize for around the time $= t + \phi \Delta t$, yielding

$$\theta(t + \Delta t) \approx \theta(t) + \Delta t(\phi \boldsymbol{Y}(t + \Delta t) + (1 - \phi)\boldsymbol{Y}(t)), \tag{3.26}$$

where the previously introduced spatial discretization is applied to the terms in $\boldsymbol{Y}$.

3.3. The overall solution scheme

In order to construct a solution, the algorithm is as follows:

- (1) *Spatio-temporal discretization*: Construct derivative terms such as

$$\frac{\partial \boldsymbol{E}(x)}{\partial x} \approx \frac{\boldsymbol{E}(x + \Delta x) - \boldsymbol{E}(x - \Delta x)}{2\Delta x}, \ \ldots \tag{3.27}$$

and insert into the governing equations: Eqs. (3.21), (3.22), (3.26). This leads to a system of coupled equations, for each node ((i, j, k) in Fig. 4), which are cast in the following (implicit/recursive) form (which are a recasting of the abstract system (Eqs. (3.1)–(3.3)))

$$\boldsymbol{E}(t + \Delta t) = \mathcal{F}(\boldsymbol{E}(t + \Delta t), \boldsymbol{H}(t + \Delta t), \theta(t + \Delta t), \ldots) \tag{3.28}$$

and

$$\boldsymbol{H}(t + \Delta t) = \mathcal{G}(\boldsymbol{E}(t + \Delta t), \boldsymbol{H}(t + \Delta t), \theta(t + \Delta t), \ldots) \tag{3.29}$$

and

$$\theta(t + \Delta t) = \mathcal{Y}(\boldsymbol{E}(t + \Delta t), \boldsymbol{H}(t + \Delta t), \theta(t + \Delta t), \ldots). \tag{3.30}$$

- (2) *System staggering:* Compute $\boldsymbol{E}$-field with $\boldsymbol{H}$ and θ fields fixed, then compute $\boldsymbol{H}$-field with $\boldsymbol{E}$ and θ fields fixed, etc., and iterate at time interval $L + 1$, $K = 1, 2, \ldots$ for

$$\boldsymbol{E}^{L+1,K} = \mathcal{F}\left(\underline{\boldsymbol{E}^{L+1,K-1}}, \boldsymbol{H}^{L+1,K-1}, \theta^{L+1,K-1}\right) \tag{3.31}$$

and

$$\boldsymbol{H}^{L+1,K} = \mathcal{G}(\boldsymbol{E}^{L+1,K}, \underline{\boldsymbol{H}^{L+1,K-1}}, \theta^{L+1,K-1}) \tag{3.32}$$

and

$$\theta^{L+1,K} = \mathcal{Y}(\boldsymbol{E}^{L+1,K}, \boldsymbol{H}^{L+1,K}, \underline{\theta^{L+1,K-1}}). \tag{3.33}$$

Solving each of the above Eqs. (3.31)–(3.33), with the respective other fields fixed, can be achieved in a variety of ways, for example iteratively or by direct (Gaussian-type) solution methods (Fig. 5). However, in theory, one could even simply perform an explicit update (no recursion). This is discussed further in the remarks that follow.

- (3) *Compute error measures*: $\varpi^{*,K} \stackrel{\text{def}}{=} max(\varpi_E^K, \varpi_H^K, \varpi_\theta^K)$, $i = 1, \ldots,$ *nodes* in the system.
- (4a) If tolerance is met, $\varpi^{*,K} \leqslant C_{tol}$ and $K \leqslant K_d$, then:
  (i) Increment time forward: $t = t + \Delta t$,
  (ii) Construct new time step: $(\Delta t)^{\text{new}} = \Phi_K \ (\Delta t)^{\text{old}}$, where
  $$\Phi_K \stackrel{\text{def}}{=} \left(\frac{\left(\frac{C_{tol}}{\varpi^{*,0}}\right)^{\frac{1}{pK_d}}}{\left(\frac{\varpi^{*,K}}{\varpi^{*,0}}\right)^{\frac{1}{pK}}} \right)$$
  (iii)
  Select $\Delta t = min((\Delta t)^{lim}, \Delta t)$ and go to (1)
- (4b) If tolerance is not met, $\varpi^{*,K} > C_{tol}$ and $K = K_d$, then construct (refine) new time step: $(\Delta t)^{\text{new}} \stackrel{\text{def}}{=} \Phi_K (\Delta t)^{\text{old}}$

$$\Phi_K \stackrel{\text{def}}{=} \left(\frac{\left(\frac{C_{tol}}{\varpi^{*,0}}\right)^{\frac{1}{pK_d}}}{\left(\frac{\varpi^{*,K}}{\varpi^{*,0}}\right)^{\frac{1}{pK}}} \right) \tag{3.34}$$

and go to (1). This adaptive time-scaling law (Zohdi et al. [53–56]) is derived in Appendix A.

At a given time, once the process is complete, then the time is incremented forward and the process is repeated. The overall goal is to deliver solutions where the iterative error is controlled and the temporal discretization accuracy dictates the upper limit on the time-step size (Δt^{lim}). Clearly, there are various combinations of solution methods that one can choose from. For example, for

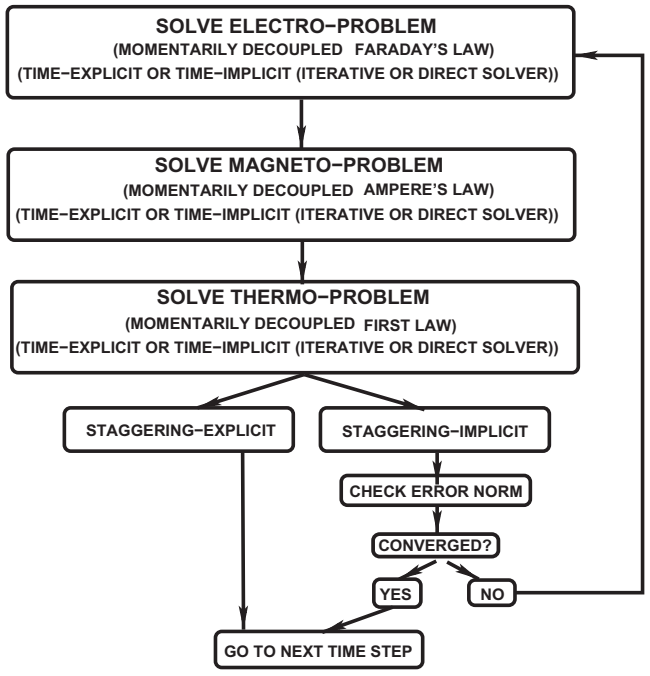

Fig. 5. Types of coupled staggering solution for the thermo–electro–magneto system.

the overall field coupling, one may choose implicit or explicit staggering and within the staggering process, either implicit ($0 < \phi \leqslant 1$) or explicit time-stepping ($\phi = 0$), and, in the case of implicit time-stepping, iterative or direct solvers for Maxwell's equations and the First Law of Thermodynamics (Fig. 5).

3.4. Discussion of the numerical scheme

There are a series of observations pertaining to the numerical scheme.

3.4.1. Comments on the staggering approach

Generally speaking, the solution to the individual field equations progresses in a node by node fashion whereby, at a node (i, j, k), for example for the magnetic field calculations, one has

$$\boldsymbol{H}(t+\Delta t)_{i,j,k} \approx \boldsymbol{\mu}^{-1}(t+\Delta t)_{i,j,k} \cdot ((\boldsymbol{\mu}\cdot\boldsymbol{H})(t)_{i,j,k} + \Delta t(\phi \boldsymbol{F}(t+\Delta t) + (1-\phi)\boldsymbol{F}(t))_{i,j,k}), \tag{3.35}$$

where the term on the lefthand side is updated and the terms on the right are previous iterate (old) values. This entails using the old values for all finite difference stencils that eventually become updated only after the algorithm completely "moves through" the system, updating values, node by node (*no matrices need to be formed*). There are a variety of techniques to accelerate such computations, such as successive over-relaxation, based on the pioneering work of Young [46]. For reviews, see Ames [4] or Axelsson [3]. Note that for the magnetic field calculations (Ampere's Law), the electric field and thermal fields are "momentarily frozen", and are updated only when it is the appropriate field's "turn" to be solved in the staggered manner. At the algebraic equation solution level, after the individual field has been solved, the entire solution is passed to the next field equation, as described in the previous algorithm (Fig. 5). This is a recursive iterative scheme of the Jacobi-type, whereby the updates are made only after one complete system iteration (as illustrated in the previous algorithm). The Jacobi method is easier to address theoretically, while the Gauss–Seidel-type method, which involves immediately using the most current field values, when they become available, is usually used at the implementation level. It is important to realize that the Jacobi method is easily parallelizable. In other words, the calculation for each node is (momentarily) uncoupled, with the updates only coming at the end of an iteration. Gauss–Seidel, since it requires the most current updates, couples the nodal calculations immediately. However, these methods can be combined to create hybrid "block-partitioned" approaches, whereby the entire domain is partitioned into subdomains and within each subdomain a Gauss–Seidel method is applied. In other words, for a subdomain, the values at all nodes from outside are initially frozen, as far as calculations involving members of the group are concerned ("block"-type calculations; see Axelsson [3]). After each isolated subdomain's solution (nodal values) has converged (computed in parallel), then all nodal values are updated, i.e. the most current values become available to all members of the grid, and the isolated subdomain calculations are repeated. Although parallel computations is not the subject of this work, some comments are also in order. Generally, interprocessor communication and synchronization is the usual bottleneck to obtain a high-performance parallel algorithm. The parallel speedup (relative to a sequential implementation), S, can be approximated by Amdahl's law (Amdahl [2]), $S = \frac{1}{1-P}$, where P is the fraction of the algorithm that is parallelizable. For example, if 40% of the code is inherently sequential, then $P = 0.6$ and $S = 2.5$. This provides an upper bound on the utility of adding more processors. A related expression is "Gustafson's law" (Gustafson [13]), $S(P) = P - k(P-1)$, where k represents the parts of the algorithm that are not parallelizable. Amdahl's law assumes that the problem is of fixed size and that the sequential part is independent of the number of processors, however, Gustafson's law does not either of these assumptions. Although we do not pursue parallel computation in the present work, we refer the reader to the works of Papadrakakis et al. [32–34] for parallel strategies that are directly applicable to the class of problems of interest, and to Stavroulakis and Papadrakakis [38] for the state-of-the-art analysis of block-parallel type calculations.

3.4.2. Comments on time-step adaptivity

Clearly, one should use the previous (converged) time step's solution as the starting guess for the next time step to obtain a "head-start" ($\boldsymbol{H}^{K=0}(t+\Delta t) = \boldsymbol{H}(t)$). When selecting a time step, one must balance accuracy concerns and, simultaneously, stability issues.[5] Clearly, the smaller the time-step, the more stable the solution process, however, more time steps means more system evaluations. One would like to keep the time steps near the (Courant–Friedrichs–Levy) CFL limit, or slightly below it. The CFL condition dictates that numerical wave speed of $\Delta x/\Delta t$ must be at least as fast as the physical wave speed (c). The electromagnetic wave speed is $c = \frac{1}{\sqrt{\epsilon_0 \mu_0}} \approx 2.997924562 \times 10^8 \pm 1.1$ m/s in vacuum while, in other media it is $c = \frac{1}{\sqrt{\epsilon\mu}}$, where the corresponding dielectric constants are ϵ and μ. Thus, since $\Delta x/\Delta t \geqslant c$, this leads to the restriction, $\Delta t \leqslant \frac{\Delta x}{c}$. Because we are dealing with heterogeneous media in three dimensions, an ad hoc, somewhat conservative, restriction is

$$\Delta t \leqslant \frac{\min(\Delta x_1, \Delta x_2, \Delta x_3)}{c_{\max}} \stackrel{\text{def}}{=} \Delta t^*, \tag{3.36}$$

where $c_{\max}$ is the fastest wave speed associated with the material components in the heterogeneous medium. Stability can, of course, be achieved by using an implicit scheme, which we employ. However, in many cases, this critical condition (for explicit methods) still serves as an indicator of poor numerical behavior, *even for implicit schemes.* For the remainder of the work, we shall refer to the "CFL number" as

$$\mathcal{CFL} \stackrel{\text{def}}{=} \Delta t \left(\frac{c_{\max}}{\min(\Delta x_1, \Delta x_2 \Delta x_3)} \right) \stackrel{\text{def}}{=} \frac{\Delta t}{\Delta t^*}. \tag{3.37}$$

Although we will not employ explicit time-stepping schemes, we refer the reader to Kunz and Luebbers [22] and Taflove and Hagness [39] for overviews, in particular on the popular Yee-scheme (Yee [45]). We remark that a critical issue in the use of explicit schemes is stability, i.e. that errors at one time step do not grow in the next time step. We refer the reader to Taflove and Hagness [39] for a detailed discussion of this topic, and detailed analysis of the Yee method, which is subject to time-step restrictions due to stability issues. We remark that, in the present work, since we shall iterate anyway due to the use of multifield staggering schemes, implicit methods are preferred for the applications of interest.

Remark. As the physics changes, the field that is most sensitive (exhibits the largest amount of relative non-dimensional change) dictates the time-step size. Because the internal system solvers within the staggering scheme are also iterative and use the previously converged solution as their starting value to solve the system of equations, a field that is relatively insensitive at given stage of the simulation will converge in a very few internal iterations (perhaps even one).

[5] Typically, the number of iterations needed to solve the coupled system, if an iterative scheme is used, increases with the time step size and the value of ϕ.

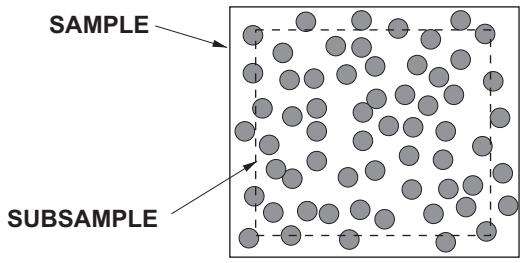

Fig. 6. With the framing method, a sample is probed with interior subsamples, within the larger sample, in order to avoid boundary effects that occur from imposing the uniform fields on the large-sample exterior.

4. Mesoscale computations

4.1. Sample size selection

Generally, in order to determine $\boldsymbol{\epsilon}^*$ (for an anisotropic overall response), one specifies three uniform (spatially constant) linearly independent loadings (either $\boldsymbol{E}$ or $\boldsymbol{D}$) on the boundary of a sample (Fig. 6).[6] Each independent loading yields three different averaged electric field components and hence provides three equations for the constitutive constants in $\boldsymbol{\epsilon}^*$. In order to determine the effective properties of the sample, one computes nine (actually 6 due to symmetry) constitutive constants $\boldsymbol{\epsilon}^*_{ij}$ in the following relation between averages (Eq. (1.1) written out)

$$\left\{\begin{array}{c}\langle D_1\rangle_\Omega\\ \langle D_2\rangle_\Omega\\ \langle D_3\rangle_\Omega\end{array}\right\}=\left[\begin{array}{ccc}\epsilon^*_{11} & \epsilon^*_{12} & \epsilon^*_{13}\\ \epsilon^*_{21} & \epsilon^*_{22} & \epsilon^*_{23}\\ \epsilon^*_{31} & \epsilon^*_{32} & \epsilon^*_{33}\end{array}\right]\left\{\begin{array}{c}\langle E_1\rangle_\Omega\\ \langle E_2\rangle_\Omega\\ \langle E_3\rangle_\Omega\end{array}\right\}. \tag{4.1}$$

If the effective response is assumed isotropic, then only one test loading (instead of usually three) is required

$$\epsilon^* \stackrel{\text{def}}{=} \sqrt{\frac{\langle \boldsymbol{D}\rangle_\Omega \cdot \langle \boldsymbol{D}\rangle_\Omega}{\langle \boldsymbol{E}\rangle_\Omega \cdot \langle \boldsymbol{E}\rangle_\Omega}}, \tag{4.2}$$

with a similar relation holding for the magnetic permeability

$$\mu^* \stackrel{\text{def}}{=} \sqrt{\frac{\langle \boldsymbol{B}\rangle_\Omega \cdot \langle \boldsymbol{B}\rangle_\Omega}{\langle \boldsymbol{H}\rangle_\Omega \cdot \langle \boldsymbol{H}\rangle_\Omega}}. \tag{4.3}$$

Since we will be dealing with materials comprised of randomly dispersed particulate media, we shall assume that the materials have an overall isotropic response and that Eqs. (4.2) and (4.3) are adequate to describe the effective material. In order to select a suitable sample that is statistically representative (a RVE), we employ a "framing" method, whereby the uniform boundary (either $\boldsymbol{E}$ or $\boldsymbol{D}$) are applied to the boundary of a sample (Fig. 6), and a subsample is used for the averaging process. This approach avoids introducing boundary layer effects into the volumetric averaging. For more details, see Zohdi et al. [53–56]. An implementation of a "framing" approach is as follows:

- *Step (1)*: Generate a sample with a certain number of particles in its interior to meet the volume fraction under investigation.
- *Step (2)*: For the effective property calculation (averaging), select a subsample ("a sub-box", Fig. 6) in the interior (to avoid boundary layer effects that arise from the imposition of uniform boundary conditions).
- *Step (3)*: Repeat Steps (1) and (2) for different random realizations for a given sample size, and average the resulting effective properties to determine a mean value.
- Step (4): Repeat Steps (1)–(4) for a larger sample.
- *Step (5)*: Continue the process (Steps (1)–(4)) until the effective property ceases to change to within an acceptable tolerance.

For a more in depth discussion on size-effect issues, see the works of Zohdi et al. [49–56].

4.2. A model problem

As a model problem, we consider a heterogeneous material combination comprised of a group of particles in a binding matrix. We generated a group of N_p randomly dispersed spherical particles, of equal size, embedded in a cubical domain of dimensions, $D \times D \times D$. The particle size was determined by a particle/sample size ratio, which was defined via a subvolume size $V \stackrel{\text{def}}{=} \frac{D\times D\times D}{N_p}$. The non-dimensional ratio between the radius (b) and the subvolume was denoted by $\mathcal{L} \stackrel{\text{def}}{=} \frac{b}{V^{\frac{1}{3}}}$. The volume fraction occupied by the particles consequently can be written as $v_p \stackrel{\text{def}}{=} \frac{4\pi\mathcal{L}^3}{3}$. Thus, the total volume occupied by the particles denoted ζ, can be written as $\zeta = v_p N_p V$. We used $N_p = 100$ particles (Fig. 7). This sample size was arrived at by successively enlarging sample until there were no significant changes in the overall system response for further enlargements. The classical random sequential addition algorithm was used to place nonoverlapping particles randomly into the domain of interest (RSA; Widom [43]). This algorithm was adequate for the volume fraction range of interest. However, if higher volume fractions are desired, more sophisticated algorithms, such as the well-known, equilibrium-based, Metropolis algorithm can be used. For even higher volume fractions (particle packing), a relatively recent class of efficient methods, based on simultaneous particle flow and growth, has been developed by Torquato and coworkers (Torquato [40], Kansaal et al. [21] and Donev et al. [9–11]).

4.3. System parameters

The following parameters were used:

- A sample size of $D \times D \times D$, with $D = 0.00005$ m, a subsample having a length-scale of $0.80 \times D$.
- An electric field on the boundary (linearly-growing), $\boldsymbol{E} = (10^9, 10^9, 10^9)\frac{t}{\bar{t}}$, initial conditions, $\boldsymbol{E}(t=0) = (0, 0, 0)$.
- A magnetic field on the boundary (linearly-growing), $\boldsymbol{H} = (10^9, 10^9, 10^9)\sqrt{\frac{\mu_o}{\epsilon_o}}\frac{t}{\bar{t}}$, initial conditions, $\boldsymbol{H} = (0, 0, 0)$.
- A time-stepping factor $\phi = 0.5$ (mid-point rule).
- A (nominal) length scale of the particles of $\zeta = 0.325$, with a ±10% variation of the resulting radius given afterwards.
- A temperature on the boundary, $\theta = 303.13$ K, and initial conditions, $\theta = 303.13$ K, along with a reference temperature of $\theta_0 = 303.13$ K.
- A relative permittivity for the particles of $\epsilon_{2r} = 50$.
- A relative permittivity for the matrix of $\epsilon_{1r} = 2$.
- A relative permeability for the particles of $\mu_{2r} = 5$.
- A relative permeability for the matrix of $\mu_{1r} = 1$.
- An electrical conductivity for the particles of $\sigma_2 = 1$.
- An electrical conductivity for the matrix of $\sigma_1 = 1$.
- A density for the particles of $\rho_2 = 2000$.
- A density of the matrix of $\rho_1 = 1000$.
- A thermal conductivity for the particles of $\mathbb{K}_2 = 200$.
- A thermal conductivity for the matrix of $\mathbb{K}_1 = 100$.
- A heat capacity for the particles of $C_2 = 2000$.
- A heat capacity for the matrix of $C_1 = 1000$.
- An absorption for the particles of $a_2 = 1$.
- An absorption for the matrix of $a_1 = 1$.

[6] In the time-transient case, the electrical and magnetic fields are coupled, and magnetic boundary data must also be supplied (either $\boldsymbol{H}$ or $\boldsymbol{B}$).

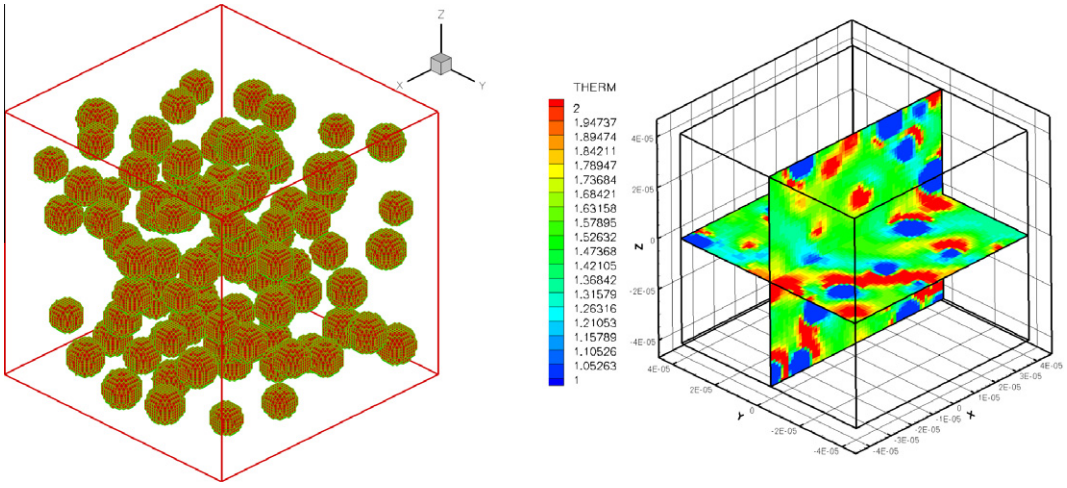

Fig. 7. Left: The morphology of the test sample's numerically-resolved microstructure, with a $101 \times 101 \times 101$ mesh which has 6,181,806 *electromagnetic degrees of freedom*. Approximately beyond the 61/81 mesh-density level there were no perceivable changes in the results. Right: the normalized temperature $\frac{\theta}{\theta_0}$.

- A (inner loop) solver tolerance, $tol = 10^{-6}$ and with the number of desired iterations per time step set to $K_d = 5$, along with a coupling/staggering tolerance of $C_{tol} = 10^{-6}$.

Remark 4. All of the Sigmoid function constants in Eqs. (1.5)–(1.9) were set to ±1;

- *for the permittivity*:
  (a) $\mathcal{K}_{E1} = 1$,
  (b) $\alpha_{E1} = 1$,
  (c) $\mathcal{K}_{E2} = 1$,
  (d) $\alpha_{E2} = 1$,
- *for the permeability:*
  (a) $\mathcal{K}_{H1} = 1$,
  (b) $\alpha_{H1} = -1$,
  (c) $\mathcal{K}_{H2} = 1$,
  (d) $\alpha_{H2} = -1$,
- *for electrical conductivity:*
  (a) $\mathcal{K}_{S1} = 1$,
  (b) $\alpha_{S1} = -1$,
  (c) $\mathcal{K}_{S2} = 1$,
  (d) $\alpha_{S2} = -1$.

Note that asymptotically, for the material behavior, as $\theta \to \infty$ and as $\|\boldsymbol{E}\| \to \infty$,

$$\mathcal{E}(\theta - \theta_R, \boldsymbol{E} - \boldsymbol{E}_R) \to (1 + \mathcal{K}_{E1} + \mathcal{K}_{E2}) \tag{4.4}$$

and

$$\sigma(\theta_R, \boldsymbol{E}_R) \to 1, \tag{4.5}$$

while as $\theta \to \infty$ and as $\|\boldsymbol{H}\| \to \infty$,

$$\mathcal{H}(\theta - \theta_R, \boldsymbol{H} - \boldsymbol{H}_R) \to 1. \tag{4.6}$$

The reference fields in the Sigmoid functions, $\boldsymbol{E}_R$ and $\boldsymbol{H}_R$, were both set to zero in the calculations.

4.4. Numerical results

For the 100 particle sample, the meshes were repeatedly refined in the following sequential manner:

1. *Mesh # 1*: a $41 \times 41 \times 41$ mesh[7] which has 413,526 *electromagnetic degrees of freedom* and 68,921 *thermodynamic degrees of freedom* for a total of 482,447 *degrees of freedom*.
2. *Mesh # 2*: a $61 \times 61 \times 61$ mesh which has 1,361,886 *electromagnetic degrees of freedom* and 226,981 *thermodynamic degrees of freedom* for a total of 1,588,867 *degrees of freedom*.
3. *Mesh # 3*: a $81 \times 81 \times 81$ mesh which has 3,188,646 *electromagnetic degrees of freedom* and 531,441 *thermodynamic degrees of freedom* for a total of 3,720,087 *degrees of freedom*.
4. *Mesh # 4:* a $101 \times 101 \times 101$ mesh which has 6,181,806 *electromagnetic degrees of freedom* and 1,030,301 *thermodynamic degrees of freedom* for a total of 7,212,107 *degrees of freedom*.

Approximately beyond the 61/81-level there were no noticeable changes in the results. *All numerical results are shown in* Figs. 7–17. At the length-scales of interest, it is questionable whether the ideas of a sharp material interface are justified. Accordingly, we simulated the system with and without Laplacian smoothing, whereby one smooths the material data by post-processing the material data, node by node, to produce a smoother material representation, for example, for the electric permittivity, $\hat{\boldsymbol{\epsilon}}$ (using the stencil in Fig. 4)

$$\nabla_x^2 \boldsymbol{\epsilon} = \boldsymbol{0} \Rightarrow \hat{\boldsymbol{\epsilon}}_{i,j,k} = \frac{1}{6}\left(\boldsymbol{\epsilon}_{i+1,j,k} + \boldsymbol{\epsilon}_{i-1,j,k} + \boldsymbol{\epsilon}_{ij+1,k} + \boldsymbol{\epsilon}_{ij-1,k} + \boldsymbol{\epsilon}_{ij,k+1} + \boldsymbol{\epsilon}_{ij,k-1}\right). \tag{4.7}$$

The same was done for the permeability by enforcing $\nabla_x^2 \boldsymbol{\mu} = \boldsymbol{0}$, as well as other material data. The simulations were run with and without data smoothing, with the results being negligibly different for sufficiently fine meshes (Fig. 7).

4.5. Observations

The effective properties for both thermally-sensitive and thermally-insensitive are shown in Figs. 7–17. Both the thermally-insensitive and thermally-sensitive cases produce effective responses which eventually fall within the bounds (using material parameters with all Sigmoid constants, the $\mathcal{K}$'s, set to zero). The thermally-sensitive case exhibits large overshoot, due to the changing properties, however, it eventually converges (saturates) to a steady-state value.

The portion of the overall field carried by each phase can be an important quantity for a material design. The "load share" of the various fields can be post processed from a direct simulation. Figs. 11–15 illustrate various overall field quantities, such as the overall electric field: $\langle \boldsymbol{E} \rangle_\Omega = \frac{1}{|\Omega|}\int_\Omega \boldsymbol{E} d\Omega$, the electric field carried by phase 1 (the matrix): $\langle \boldsymbol{E} \rangle_{\Omega_1} = \frac{1}{|\Omega_1|}\int_{\Omega_1} \boldsymbol{E} d\Omega$ and the electric field

[7] A $41 \times 41 \times 41$ arises from having a cubical mesh with 20 nodes from the centerline line/plane of symmetry and one node in the middle.

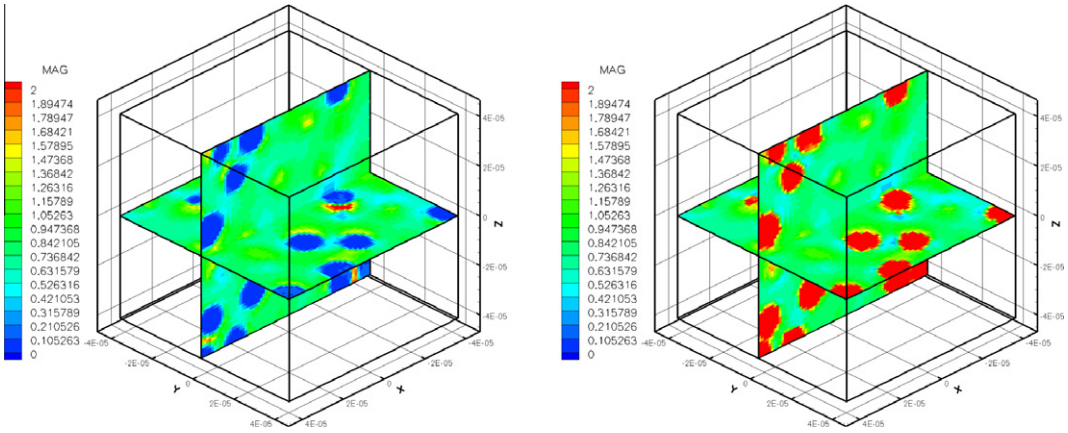

Fig. 8. Left: The normalized electric field, $\frac{\boldsymbol{E}}{\|\boldsymbol{E}_o\|}$. Right: The normalized electric field flux, $\frac{\boldsymbol{D}}{\epsilon_0\|\boldsymbol{E}_o\|}$.

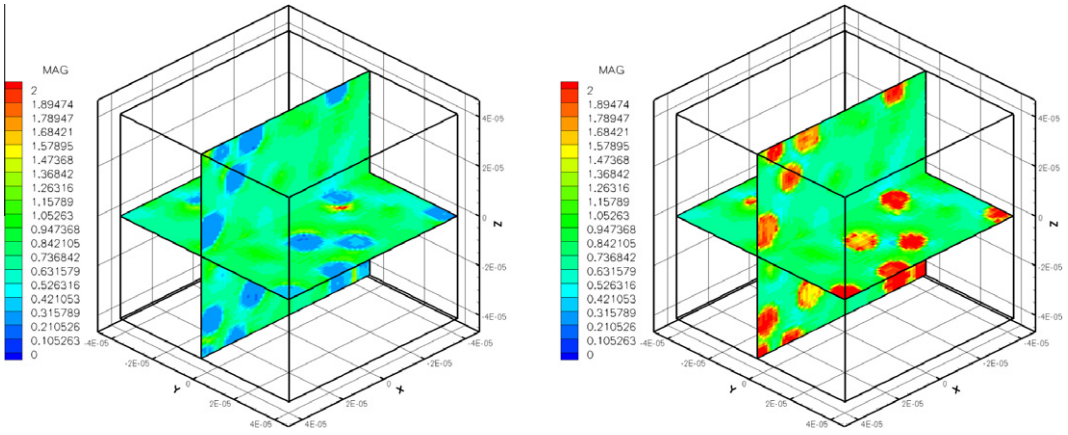

Fig. 9. Left: The normalized magnetic field, $\frac{\boldsymbol{H}}{\|\boldsymbol{H}_o\|}$. Right: The normalized magnetic field flux, $\frac{\boldsymbol{B}}{\mu_0\|\boldsymbol{H}_o\|}$.

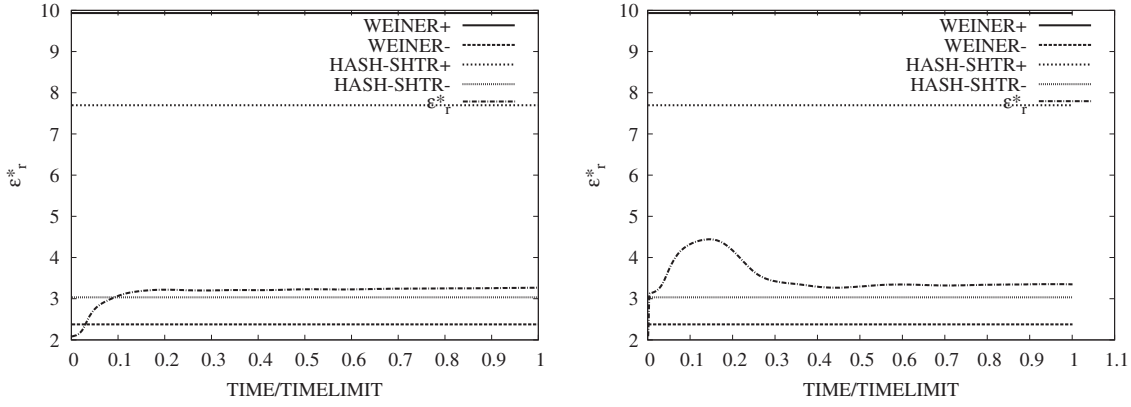

Fig. 10. The *isotropic* effective permittivity (ϵ^*). Left: Thermally-insensitive case. Right: Thermally-sensitive case. *Note*: The analytical bounds that are shown, are based on expressions having all constants set to zero in the Sigmoid functions.

carried by phase 2 (the particles): $\langle \boldsymbol{E}\rangle_{\Omega_2} = \frac{1}{|\Omega_2|}\int_{\Omega_2} \boldsymbol{E}d\Omega$, as well as the other quantities such as $\boldsymbol{D}$, $\boldsymbol{H}$ and $\boldsymbol{B}$. Note that

$$\langle \boldsymbol{E}\rangle_{\Omega} = \frac{1}{|\Omega|}\left(\int_{\Omega_1} \boldsymbol{E}d\Omega + \int_{\Omega_2} \boldsymbol{E}d\Omega\right) = v_1^{\epsilon}\langle \boldsymbol{E}\rangle_{\Omega_1} + v_2^{\epsilon}\langle \boldsymbol{E}\rangle_{\Omega_2} \tag{4.8}$$

and

$$\langle \boldsymbol{D}\rangle_{\Omega} = \frac{1}{|\Omega|}\left(\int_{\Omega_1} \boldsymbol{D}d\Omega + \int_{\Omega_2} \boldsymbol{D}d\Omega\right) = v_1^{\epsilon}\langle \boldsymbol{D}\rangle_{\Omega_1} + v_2^{\epsilon}\langle \boldsymbol{D}\rangle_{\Omega_2}. \tag{4.9}$$

As illustrated in Fig. 17, we note that the time steps were initially set to be the CFL limit $\mathcal{CFL} = 1$, but had to be refined below that level for the thermally-sensitive case. Unrefinements also took place, when allowable (if below the upper time-step limit). The coupling tolerance was set to $C_{tol} = 10^{-6}$ in the preceding calculations. Only the thermally-sensitive problems required time-step adaptivity (below the CFL limit) to control the coupling error. However, if the C_{tol} was made coarser, for example to $C_{tol} = 10^{-5}$ and $C_{tol} = 10^{-4}$, etc., eventually the *CFL*-time step would have been adequate for the

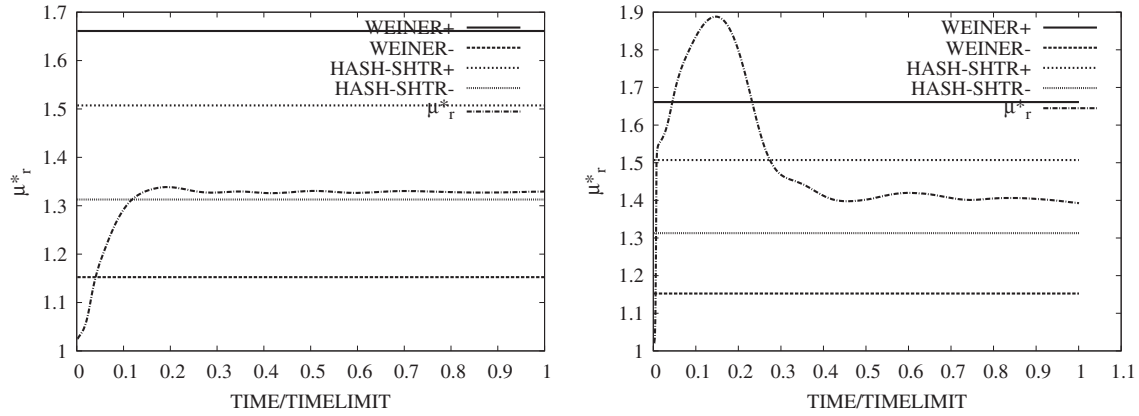

Fig. 11. The *isotropic* effective permeability ($\boldsymbol{\mu}^*$). Left: Thermally-insensitive case. Right: Thermally-sensitive case. *Note*: The analytical bounds that are shown, are based on expressions having all constants set to zero in the Sigmoid functions.

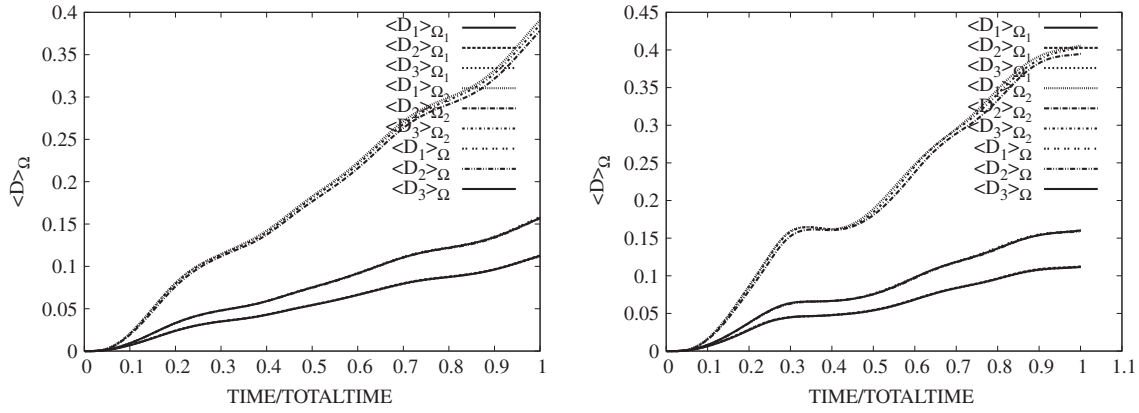

Fig. 12. The volume averaged electric flux: (1) carried by the particles $\langle \boldsymbol{D} \rangle_{\Omega_2}$ (top curves), (2) carried by the matrix $\langle \boldsymbol{D} \rangle_{\Omega_1}$ (bottom curves) and (3) overall $\langle \boldsymbol{D} \rangle_{\Omega}$ (middle curves). Left: Thermally-insensitive case. Right: Thermally-sensitive case. In all the cases, the overall average of the $\boldsymbol{D}$-components in each phase are virtually identical (equal in all three directions, as expected due to the equi-axial boundary loading), i.e. the overall response (ϵ^*) is isotropic.

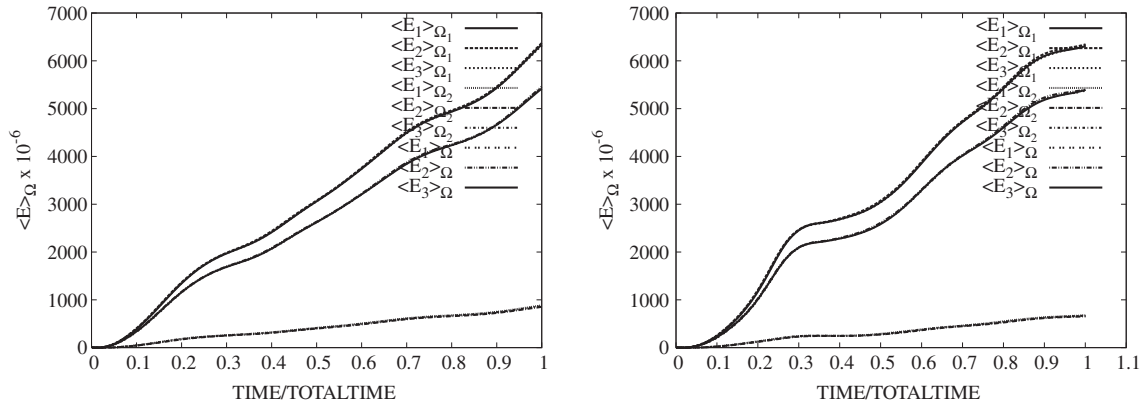

Fig. 13. The volume averaged electric field: (1) carried by the particles $\langle \boldsymbol{E} \rangle_{\Omega_2}$ (bottom curves), (2) carried by the matrix $\langle \boldsymbol{E} \rangle_{\Omega_1}$ (top curves) and (3) overall $\langle \boldsymbol{E} \rangle_{\Omega}$ (middle curves). Left: Thermally-insensitive case. Right: Thermally-sensitive case. In all the cases, the overall average of the $\boldsymbol{E}$-components in each phase are virtually identical (equal in all three directions, as expected due to the equi-axial boundary loading), i.e. the overall response (ϵ^*) is isotropic.

thermally-sensitive case, as for the thermally-insensitive case. Clearly, these results are dependent on the material parameters selected. It is important to stress that it is virtually impossible to determine a priori whether the initial time step is adequate to meet a tolerance and whether adaptivity is needed. *Obviously, we can use this scheme for any (trapezoidal) value of* $0 \leqslant \phi \leqslant 1$. Time-step size adaptivity is important, since the solution can dramatically change over the course of time, possibly requiring quite different time-step sizes to control the iterative (staggering) error. However, to maintain the accuracy of the time-stepping scheme, one must respect an upper bound dictated by the discretization error, i.e., $\Delta t \leqslant \Delta t^{lim}$ (and the CFL condition). As stated before, classical solution methods require $\mathcal{O}(N^3)$ operations, whereas iterative schemes, such as the one presented, typically require order N^q, where $1 \leqslant q \leqslant 2$. For de-

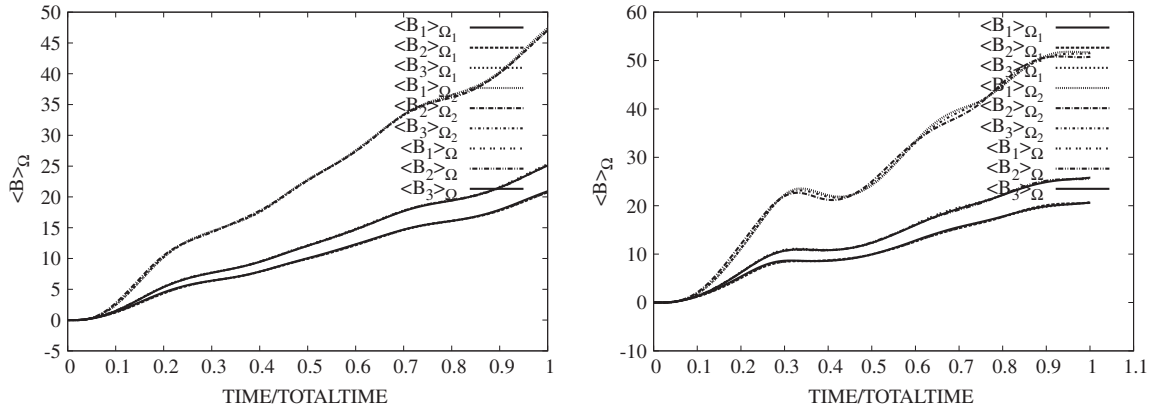

Fig. 14. The volume averaged magnetic flux: (1) carried by the particles $\langle \boldsymbol{B} \rangle_{\Omega_2}$ (top curves), (2) carried by the matrix $\langle \boldsymbol{B} \rangle_{\Omega_1}$ (bottom curves) and (3) overall $\langle \boldsymbol{B} \rangle_{\Omega}$ (middle curves). Left: Thermally-insensitive case. Right: Thermally-sensitive case. In all the cases, the overall average of the $\boldsymbol{D}$-components in each phase are virtually identical (equal in all three directions, as expected due to the equi-axial boundary loading), i.e. the overall response ($\boldsymbol{\mu}^*$) is isotropic.

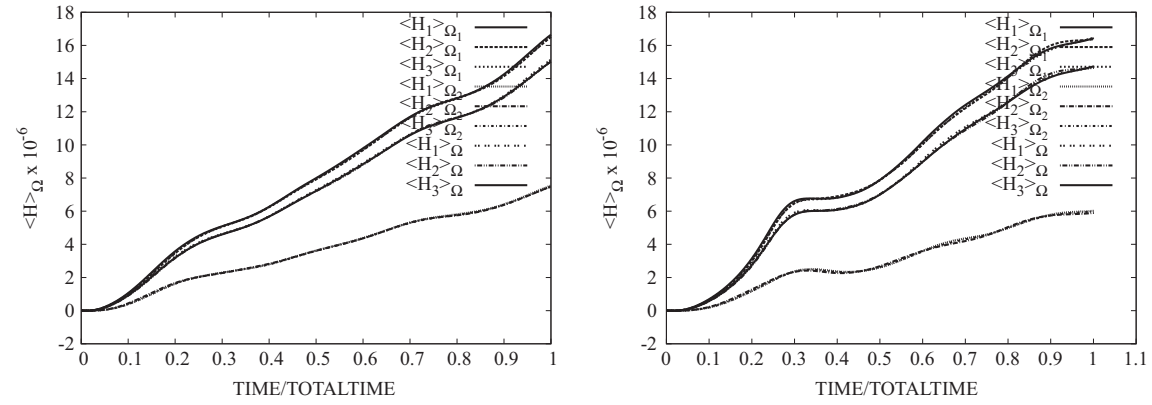

Fig. 15. The volume averaged magnetic field: (1) carried by the particles $\langle \boldsymbol{H} \rangle_{\Omega_2}$ (bottom curves), (2) carried by the matrix $\langle \boldsymbol{H} \rangle_{\Omega_1}$ (top curves) and (3) overall $\langle \boldsymbol{H} \rangle_{\Omega}$ (middle curves). Left: Thermally-insensitive case. Right: Thermally-sensitive case. In all the cases, the overall average of the $\boldsymbol{H}$-components in each phase are virtually identical (equal in all three directions, as expected due to the equi-axial boundary loading), i.e. the overall response ($\boldsymbol{\mu}^*$) is isotropic.

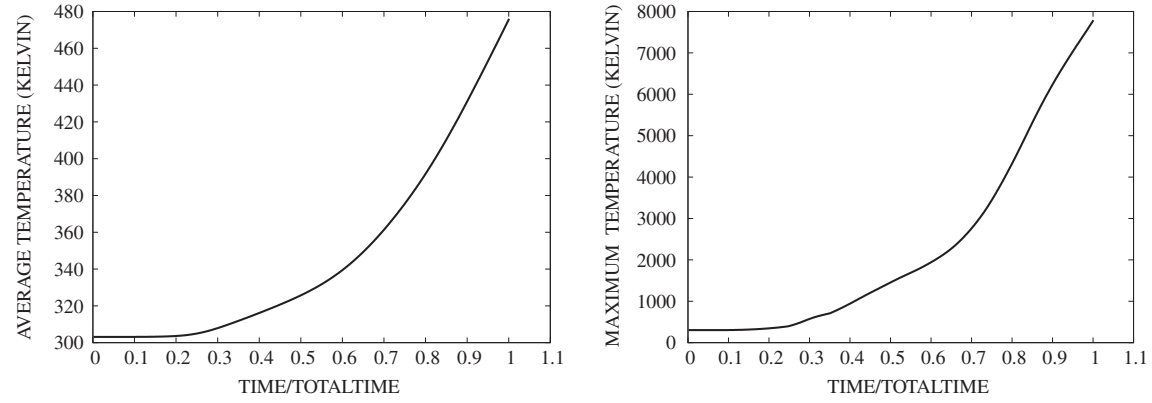

Fig. 16. Left: Average temperature ($\langle \theta \rangle_{\Omega}$). Right: The maximum temperature, for the thermally-sensitive case.

tails see Axelsson [3]. Also, such solvers are highly advantageous since solutions to previous time steps can be used as the first guess to accelerate the solution procedure.

5. Stress- and chemically-induced damage

The generation of heat and stress (due to Joule heating and electromagnetically-induced body forces) can initiate forms of damage that are both mechanically-induced and chemically-induced. Accordingly, we now formulate extensions, involving stress- and chemically-induced degradation by enlarging the formulation to multifield systems to include simultaneous time-transient solution of: (1) Maxwell's equations, (2) the First Law of Thermodynamics, (3) the balance of linear momentum and (4) reaction–diffusion laws.

Remark 1. We consider regimes where *infinitesimal deformations are appropriate*. Consistent with the infinitesimal deformation approximation, where X are referential coordinates, x are current coordinates and $\nabla_x(\cdot) \approx \nabla_X(\cdot)\left(\frac{\partial(\cdot)}{\partial \boldsymbol{x}} \approx \frac{\partial(\cdot)}{\partial \boldsymbol{X}}\right)$. The mechanical displacement is given by $u = x - X$, and time derivatives given by

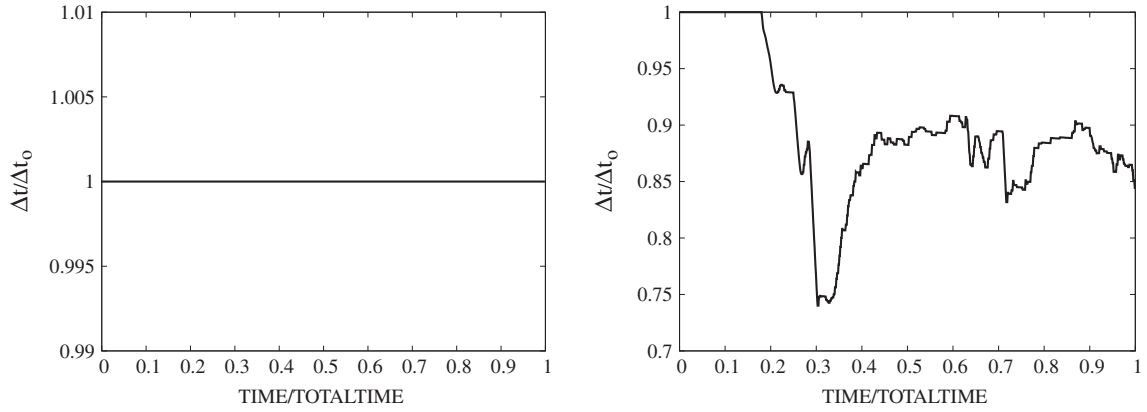

Fig. 17. Time-step size relative to the $\mathcal{CFL}$-limit size (constant for the uncoupled problem). Left: Thermally-insensitive case. Right: Thermally-sensitive case. The time steps were initially set to be the CFL limit $\mathcal{CFL} \stackrel{\text{def}}{=} \Delta t\left(\frac{c_{\max}}{\min(\Delta x_1, \Delta x_2, \Delta x_3)}\right) = 1$, but had to be refined below that level.

$$\dot{(\,)} = \frac{d(\,)}{dt} = \frac{\partial(\,)}{\partial t}\bigg|_X + \nabla_X(\,) \cdot \underbrace{\frac{d\boldsymbol{X}}{dt}}_{=0} = \frac{\partial(\,)}{\partial t}\bigg|_X. \tag{5.1}$$

In addition to simplification some of the governing equations pertaining to the system thermodynamics, linear momentum and chemical reactions, the curl equations in Maxwell's equations effectively becomes $\nabla_x \times (\cdot) \approx \nabla_X \times\ (\cdot)$.

Remark 2. One may compute the induced mechanical loads by computing $\boldsymbol{f} = \mathcal{P}\boldsymbol{E} + \boldsymbol{J}^{tot} \times \boldsymbol{B}$, where $\mathcal{P}$ is the charge per unit volume, computed from the divergence form of Faraday's law, $\nabla_x \cdot \boldsymbol{D} = \mathcal{P}$, for use in an electromagnetic stress analysis, where

$$\nabla_x \cdot \boldsymbol{T} + \boldsymbol{f} = \rho \frac{d^2\boldsymbol{u}}{dt^2}, \tag{5.2}$$

T being the Cauchy stress.

Remark 3. Note, for a deforming medium, in the Faraday's law, the term $\sigma \cdot E$ becomes $\sigma \cdot\ (E + v \times B)$.

5.1. Damage evolution

Within the framework of *infinitesimal deformations*, we consider a mechanical isotropic damage constitutive law given by

$$\boldsymbol{T} = \alpha \mathbb{E}_0 : (\boldsymbol{\epsilon} - \boldsymbol{\beta}), \tag{5.3}$$

where $\boldsymbol{T}$ is the Cauchy stress, governed by a balance of linear momentum[8]

$$\nabla_x \cdot \boldsymbol{T} + \boldsymbol{f} = \rho \ddot{\boldsymbol{u}} \tag{5.4}$$

which under infinitesimal deformation framework becomes

$$\nabla_X \cdot \boldsymbol{T} + \boldsymbol{f} = \rho_o \frac{\partial^2 \boldsymbol{u}}{\partial \boldsymbol{t}^2}, \tag{5.5}$$

or, explicitly,

$$\nabla_X \cdot (\Lambda \mathbb{E}_0 : (\boldsymbol{\varepsilon} - \boldsymbol{\beta})) + \boldsymbol{f} = \rho_o \frac{\partial^2 \boldsymbol{u}}{\partial \boldsymbol{t}^2} \tag{5.6}$$

with infinitesimal strains given by $\boldsymbol{\varepsilon} = \frac{1}{2}(\nabla_X \boldsymbol{u} + (\nabla_X \boldsymbol{u})^T)$ and thermal strains given by $\boldsymbol{\beta} = \boldsymbol{\varepsilon}_\theta \stackrel{\text{def}}{=} \boldsymbol{\gamma} \cdot (\theta - \theta_0)\boldsymbol{1}$. Here, the (isotropic) damaged elasticity tensor is $\mathbb{E} = \alpha \mathbb{E}_0$, where $\mathbb{E}_0$ represents the "virgin" isotropic undamaged material, $0 \leqslant \Lambda \leqslant 1$ is the scalar continuity (isotropic damage) parameter (Kachanov [20]), $\Lambda(t = 0) = 1$ indicates the initial undamaged state and $\Lambda \to 0$ indicates a completely damaged state. The damage arising from mechanical and chemical sources is modeled as being governed by evolution over-stress functions of the form $(0 < \Lambda \leqslant 1)$

$$\dot{\Lambda} = \Bigg(\underbrace{a_1|\dot{c}|}_{\text{chemistry}} + \underbrace{a_2 H\left(\frac{|tr\boldsymbol{T}/3|}{|tr\boldsymbol{T}_{crit}/3|} - 1\right)\left(\frac{|tr\boldsymbol{T}/3|}{|tr\boldsymbol{T}_{crit}/3|} - 1\right)}_{\text{dilatation}} + \underbrace{a_3 H\left(\frac{\|\boldsymbol{T}'\|}{\|\boldsymbol{T}'_{crit}\|} - 1\right)\left(\frac{\|\boldsymbol{T}'\|}{\|\boldsymbol{T}'_{crit}\|} - 1\right)}_{\text{deviator}} \Bigg) \Lambda, \tag{5.7}$$

where the normalized concentration of the solute is c, given in molecules per unit volume, where $\boldsymbol{T}'_{crit} \stackrel{\text{def}}{=} k_1 \frac{\boldsymbol{T}'}{\|\boldsymbol{T}'\|}, \frac{tr\boldsymbol{T}_{crit}}{3} \stackrel{\text{def}}{=} k_2$, k_1 and k_2 being material constants, $\boldsymbol{T}' = \boldsymbol{T} - \frac{tr\boldsymbol{T}}{3}\boldsymbol{1}$. $H(\cdot)$ is the Heaviside function that is equal to zero when the argument is negative and is equal to unity otherwise. The material parameters (rate constants) a_1–a_3 and k_1 and k_2 are spatially variable (different for each phase). For further details on these types of phenomenological (damage) formulations, the interested reader is referred to the seminal work of Kachanov [20]. Clearly, further evolution laws can be written for other material property changes, such as the thermal conductivity and dielectric properties, although only changes in the mechanical property $\mathbb{E}$ are considered during the formulations to follow.[9]

5.2. Modification of the First Law of Thermodynamics

For a referential formulation of the First Law of Thermodynamics, we make the following infinitesimal strain approximation, for the stored energy

$$\rho_o w = W \approx \frac{1}{2}(\boldsymbol{\varepsilon} - \boldsymbol{\beta}) : \mathbb{E} : (\boldsymbol{\varepsilon} - \boldsymbol{\beta}) + \rho_o C\theta, \tag{5.8}$$

which implies

$$\rho_o \dot{w} = \dot{W} = \frac{1}{2}(\boldsymbol{\varepsilon} - \boldsymbol{\beta}) : \dot{\mathbb{E}} : (\boldsymbol{\varepsilon} - \boldsymbol{\beta}) + (\dot{\boldsymbol{\varepsilon}} - \dot{\boldsymbol{\beta}}) : \mathbb{E} : (\boldsymbol{\varepsilon} - \boldsymbol{\beta}) + \rho_o C\dot{\theta}, \tag{5.9}$$

[8] The body force represents the electromagnetic coupling term, $\boldsymbol{f} = \mathcal{P}\boldsymbol{E} + \boldsymbol{J}^{tot} \times \boldsymbol{B}$.

[9] In the case of material isotropy, $\mathbb{E} : \boldsymbol{\epsilon} = \lambda tr\boldsymbol{\epsilon} + 2\mu\boldsymbol{\epsilon}$, where λ is the Lame parameter and μ is the shear modulus.

and thus the first law becomes

$$\rho_o C\dot{\theta} = \boldsymbol{T} : \dot{\boldsymbol{\beta}} - \frac{1}{2}(\boldsymbol{\varepsilon} - \boldsymbol{\beta}) : \dot{\mathbb{E}} : (\boldsymbol{\varepsilon} - \boldsymbol{\beta}) + \nabla_X \cdot (\mathbb{K} \cdot \nabla_X \theta) + \rho_o z, \quad (5.10)$$

where Fourier's law, $\boldsymbol{q} = -\mathbb{K} \cdot \nabla_X \theta$, has been employed.

Remark. The chemical production of energy at a point is modeled as being related to the change in the rate of reaction, $\rho_o z = \eta|\dot{c}|$, which is discussed in detail in the next section, where η is a spatially variable material parameter. The parameter η is positive for exothermic reactions and negative for endothermic reactions.

5.3. Solid-state diffusion–reaction

The mass balance for a small diffusing species, denoted by the normalized concentration of the solute c (molecules per unit volume), in an arbitrary subvolume of material contained within Ω, denoted ω, consists of a storage term ($\dot{c}$), a reaction term ($\dot{s}$), and an inward normal flux term ($-\boldsymbol{q}_c \cdot \boldsymbol{n}$), leading to

$$\int_\omega (\dot{c} + \dot{s}) d\omega = -\int_{\partial\omega} \boldsymbol{q}_c \cdot \boldsymbol{n}\, da. \quad (5.11)$$

It is a classical *stoichiometrically inexact* approximation to assume that the diffusing species reacts (is created or destroyed) in a manner such that the rate of production of the reactant (s) is directly proportional to the concentration of solute (c) itself and the rate of change of the solute (c) species,

$$\dot{s} = \tau_1 c + \tau_2 \dot{c}. \quad (5.12)$$

Here, $\tau_1 = r_1 e^{-\frac{Q_1}{R\theta}}$ and $\tau_2 = r_2 e^{-\frac{Q_2}{R\theta}}$, where r_1 and r_2 are rate constants, Q_1 and Q_2 are activation energies per mole of diffusive species, R is the universal gas constant and θ is the temperature in degrees Kelvin. Upon substitution of these relations into the conservation law for the diffusing species, and after using the divergence theorem, since the volume ω is arbitrary, one has a Fickian diffusion–reaction model in strong form, assuming a Fickian-type law, $\boldsymbol{q}_c = -\mathbb{D} \cdot \nabla_X c$

$$\begin{aligned}\dot{c} &= \nabla_X \cdot (\mathbb{D} \cdot \nabla_X c) - \tau_1 c - \tau_2 \dot{c} \Rightarrow \dot{c}(1 + \tau_2) \\ &= \nabla_X \cdot (\mathbb{D} \cdot \nabla_X c) - \tau_1 c, \end{aligned} \quad (5.13)$$

where, as before, $\dot{(\,)} = \frac{\partial (\,)}{\partial t}|_X$. When $r_1 > 0$, the diffusing species is destroyed as it reacts, while $r_1 < 0$ indicates that the diffusing species is created as it reacts, i.e. an autocatalytic or "chain" reaction occurs. Also, depending on the sign of r_2, effectively the process will have an accelerated or decelerated diffusivity as well as accelerated or decelerated reactivity. In Eq. (5.13), the familiar Arrhenius form $\mathbb{D} = \mathbb{D}_0 e^{-\frac{U}{R\theta}}$ has been used, where $\mathbb{D}_0$ is the diffusivity tensor at a reference temperature, U is the activation energy per mole of diffusive species.

Remark 1. It is sometimes observed that, in regions of relatively high positive triaxial stress, the diffusion is accelerated, while in regions of high negative triaxial stress, diffusion is decelerated. Diffusion models with explicit pressure dependency will not be considered, however, we remark that a particularly simple constitutive model to incorporate stress-dependency phenomena is given by a pseudo-Fickian/Arrhenius law, $\boldsymbol{q}_c = -\mathbb{D}_0 e^{\frac{-U(\boldsymbol{T})}{R\theta}} \cdot \nabla c$, motivated by thermodynamical arguments found in the classical works of Flynn [12] or Crank [6].[10]

Remark 2. It is important to note that instabilities can be induced by diffusion, i.e. a coupled mechano-chemical system can be stable when no diffusion is present and unstable in the presence of diffusion. An indepth mathematical analysis of such effects has been conducted by Markenscoff [25–27].

5.4. Discretization of the mechanical and concentration fields

5.4.1. Mechanical field

For the mechanical field (infinitesimal deformation formulation) we write ($\boldsymbol{v} = \dot{\boldsymbol{u}}$ is the velocity)

$$\frac{d\boldsymbol{v}}{dt} = \frac{\partial \boldsymbol{v}}{\partial t} = \frac{1}{\rho_o}(\nabla_X \cdot \boldsymbol{T} + \boldsymbol{f}) \stackrel{\text{def}}{=} \boldsymbol{L}. \quad (5.14)$$

We discretize for time = $t + \phi\Delta t$, and using a trapezoidal "ϕ-scheme" ($0 \leqslant \phi \leqslant 1$, see Appendix)

$$\frac{\boldsymbol{v}(t + \Delta t) - \boldsymbol{v}(t)}{\Delta t} \approx \boldsymbol{L}(t + \phi\Delta t) \approx \phi \boldsymbol{L}(t + \Delta t) + (1 - \phi)\boldsymbol{L}(t). \quad (5.15)$$

Rearranging, yields

$$\boldsymbol{v}(t + \Delta t) \approx \boldsymbol{v}(t) + \Delta t(\phi \boldsymbol{L}(t + \Delta t) + (1 - \phi)\boldsymbol{L}(t)), \quad (5.16)$$

where the previously introduced spatial discretization is applied to the terms in $\boldsymbol{L}$ ($\nabla_x \cdot \boldsymbol{T}$). Since this is a second-order system, the procedure is then repeated to determine the displacement field $\boldsymbol{u}$ (see Appendix D).

Remark. As in our treatment of Maxwell's equations, finite difference stencils are used (with additional mixed derivatives), and the details are given in Appendix C.

5.4.2. Chemical field

For the concentration field we write

$$\frac{\partial c}{\partial t} = \frac{1}{1 + \tau_2}(-\nabla_X \cdot \boldsymbol{q}_c - \tau_2 c) \stackrel{\text{def}}{=} \boldsymbol{Z}. \quad (5.17)$$

We discretize for around the time = $t + \phi\Delta t$, yielding

$$c(t + \Delta t) \approx c(t) + \Delta t(\phi \boldsymbol{Z}(t + \Delta t) + (1 - \phi)\boldsymbol{Z}(t)), \quad (5.18)$$

where the previously introduced spatial discretization is applied to the terms in $\boldsymbol{q}_c$.

5.5. Extended numerics: staggering for electro–magneto–thermo–mechano–chemo systems

Extending the previous electro–magneto–thermo staggering scheme to include mechanical and chemical effects, one computes the $\boldsymbol{E}$-field with $\boldsymbol{H}$, θ, $\boldsymbol{u}$ and c fields fixed, then computes $\boldsymbol{H}$-field with $\boldsymbol{E}$, θ, $\boldsymbol{u}$ and c fields fixed, etc., and iterates at time interval $L + 1$, $K = 1, 2, \ldots$ for (written directly in iterative implicit form)

$$\boldsymbol{E}^{L+1,K} = \mathcal{F}\left(\underline{\boldsymbol{E}^{L+1,K-1}}, \boldsymbol{H}^{L+1,K-1}, \theta^{L+1,K-1}, \boldsymbol{u}^{L+1,K-1}, c^{L+1,K-1}\right) \quad (5.19)$$

and

$$\boldsymbol{H}^{L+1,K} = \mathcal{G}\left(\boldsymbol{E}^{L+1,K}, \underline{\boldsymbol{H}^{L+1,K-1}}, \theta^{L+1,K-1}, \boldsymbol{u}^{L+1,K-1}, c^{L+1,K-1}\right) \quad (5.20)$$

and

$$\theta^{L+1,K} = \mathcal{Y}\left(\boldsymbol{E}^{L+1,K}, \boldsymbol{H}^{L+1,K}, \underline{\theta^{L+1,K-1}}, \boldsymbol{u}^{L+1,K-1}, c^{L+1,K-1}\right) \quad (5.21)$$

and

$$\boldsymbol{u}^{L+1,K} = \mathcal{L}\left(\boldsymbol{E}^{L+1,K}, \boldsymbol{H}^{L+1,K}, \theta^{L+1,K}, \underline{\boldsymbol{u}^{L+1,K-1}}, c^{L+1,K-1}\right) \quad (5.22)$$

and

$$c^{L+1,K} = \mathcal{C}\left(\boldsymbol{E}^{L+1,K}, \boldsymbol{H}^{L+1,K}, \theta^{L+1,K}, \boldsymbol{u}^{L+1,K}, \underline{c^{L+1,K-1}}\right), \quad (5.23)$$

[10] An additive split for stress dependency of the form $U(\boldsymbol{T}) = U_0 + \widetilde{U}(p)$, where U_0 is a stress-independent reference activation energy and $p = \frac{tr\boldsymbol{T}}{3}$ is the pressure, has been given in Zohdi [57–59] for certain applications.

where the only underlined variable is "active" at that stage of the process. One then compute error measures: $\varpi^{*,K} \stackrel{\text{def}}{=} max\left(\varpi_E^K, \varpi_H^K, \varpi_\theta^K, \varpi_u^K, \varpi_c^K\right), i = 1, \ldots, nodes$ in the system, where, in addition to the previously introduced *non-dimensional* errors for the electric, magnetic and thermal fields, we define, for the displacement

$$\varpi_u^K \stackrel{\text{def}}{=} \frac{\|\boldsymbol{u}^{L+1,K} - \boldsymbol{u}^{L+1,K-1}\|}{\|\boldsymbol{u}^{L+1,K} - \boldsymbol{u}^{L}\|} \tag{5.24}$$

and for the concentration

$$\varpi_c^K \stackrel{\text{def}}{=} \frac{\|c^{L+1,K} - c^{L+1,K-1}\|}{\|c^{L+1,K} - c^{L}\|}. \tag{5.25}$$

Thereafter, we select the maximum error for adaptivity

$$\varpi^{*,K} \stackrel{\text{def}}{=} max\left(\varpi_E^K, \varpi_H^K, \varpi_\theta^K, \varpi_u^K, \varpi_c^K\right) \tag{5.26}$$

and proceed as introduced earlier for the electro–magneto–thermo scheme, with the modified flowchart shown in Fig. 18.

Remark 1. An electro–magneto–thermo–mechano–chemo numerical example is provided in Appendix E.

Remark 2. Because the temperatures can become quite high (as seen in Figs. 7–17), especially without a cooling mechanism, one may wish to include phase transformations by considering four cases:

- *No melting*: If $\theta(t) < \theta_m$ and $\theta(t + \Delta t) < \theta_m$, then $C(\theta) = C_0$, where C_0 is the solid heat capacity.
- *Melting*: If $\theta(t) < \theta_m$ and $\theta(t + \Delta t) \geqslant \theta_m$, then $C(\theta) = C_o + \frac{\Delta H_m^{S\to L}}{\Delta\theta_m}$, where $\Delta H_m^{S\to L}$ is the latent heat of melting. This has the effect of enforcing a constant temperature (or absorbing the latent heat), where $\Delta\theta_m$ is small and can be thought of as a "band-width" for melting.
- *Melted*: If $\theta(t) \geqslant \theta_m$ and $\theta(t + \Delta t) \geqslant \theta_m$, then $C(\theta) = C_m$, where C_m is the heat capacity of the melted material.
- *Solidification*: If $\theta(t) \geqslant \theta_m$ and $\theta(t + \Delta t) < \theta_m$, then $C(\theta) = C_m + \frac{\Delta H_m^{L\to S}}{\Delta\theta_m}$, where $\Delta H_m^{L\to S}$ is the latent heat of solidification.

This is relatively straightforward to include within the staggering framework.

6. Summary

The overall goal was to deliver solutions where the iterative staggering (incomplete coupling) error is controlled and the temporal discretization accuracy dictates the upper limits on the time-step size (Δt^{lim}). Generally speaking, the staggering error, which is a function of the time-step size, is time-dependent and can become stronger, weaker, or possibly oscillatory, is extremely difficult to ascertain a priori as a function of the time-step size. Therefore, to circumvent this problem, the presented adaptive staggering strategy was developed to provide accurate solutions by iteratively adjusting the time steps. Specifically, a sufficient condition for the convergence of the presented fixed-point scheme was that the spectral radius (contraction constant of the coupled operator), which depends on the time-step size, must be less than unity. This observation was used to adaptively control the time-step sizes, while simultaneously controlling the coupled operator's spectral radius, in order to deliver solutions below an error tolerance within a prespecified number of desired iterations. This recursive staggering error control can allow for substantial reduction of computational effort by the adaptive use of large time steps, when possible. Furthermore, such a recursive process has a reduced sensitivity (relative to an explicit staggering approach) to the order in which the individual equations are solved, since it is self-correcting.

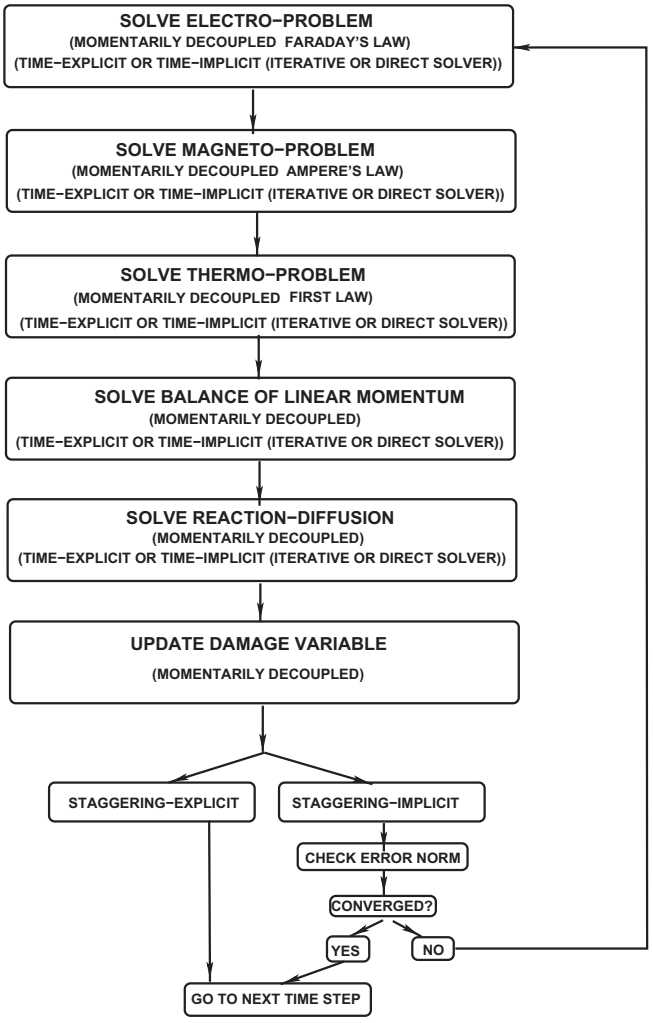

Fig. 18. Types of coupled staggering solution for the thermo–electro–magneto–mechano–chemo system.

Appendix A. Temporally-adaptive iterative methods

Implicit time-stepping methods, with time-step size adaptivity, built on approaches found in Zohdi [53–56], were used throughout the analysis in the body of the work. In order to introduce basic concepts, we consider a first-order differential equation

$$\mathcal{M}\dot{\boldsymbol{U}} = \boldsymbol{F}(\boldsymbol{U}), \tag{8.1}$$

which, after being discretized using a trapezoidal "ϕ-method" $(0 \leqslant \phi \leqslant 1)$

$$\boldsymbol{U}^{L+1} = \boldsymbol{U}^{L} + \frac{\Delta t}{\mathcal{M}}\left(\phi \boldsymbol{F}(\boldsymbol{U}^{L+1}) + (1-\phi)\boldsymbol{F}(\boldsymbol{U}^{L})\right). \tag{8.2}$$

A straightforward iterative scheme can be written as

$$\boldsymbol{U}^{L+1,K} = \mathcal{G}(\boldsymbol{U}^{L+1,K-1}) + \mathcal{R}, \tag{8.3}$$

where $\mathcal{R}$ is a remainder term that does not depend on the solution, i.e. $\mathcal{R} \neq \mathcal{R}(\boldsymbol{U}^{L+1})$, and $K = 1, 2, 3, \ldots$ is the index of iteration within time step $L + 1$. The convergence of such a scheme is dependent on the behavior of $\mathcal{G}$. Namely, a sufficient condition for convergence

is that $\mathcal{G}$ is a contraction mapping for all $\boldsymbol{U}^{L+1,K}$, $K = 1, 2, 3, \ldots$ In order to investigate this further, we define the iteration error as

$$\varpi^{L+1,K} \stackrel{\text{def}}{=} \boldsymbol{U}^{L+1,K} - \boldsymbol{U}^{L+1}. \tag{8.4}$$

A necessary restriction for convergence is iterative self consistency, i.e. the "exact" (discretized) solution must be represented by the scheme

$$\mathcal{G}(\boldsymbol{U}^{L+1}) + \mathcal{R} = \boldsymbol{U}^{L+1}. \tag{8.5}$$

Enforcing this restriction, a sufficient condition for convergence is the existence of a contraction mapping

$$\varpi^{L+1,K} = \|\boldsymbol{U}^{L+1,K} - \boldsymbol{U}^{L+1}\| = \|\mathcal{G}(\boldsymbol{U}^{L+1,K-1}) - \mathcal{G}(\boldsymbol{U}^{L+1})\|, \tag{8.6}$$

$$\leqslant \eta^{L+1,K}\|\boldsymbol{U}^{L+1,K-1} - \boldsymbol{U}^{L+1}\|, \tag{8.7}$$

where, if $0 \leqslant \eta^{L+1,K} < 1$ for each iteration K, then $\varpi^{L+1,K} \to \boldsymbol{0}$ for any arbitrary starting value $\boldsymbol{U}^{L+1,K=0}$, as $K \to \infty$. This type of contraction condition is sufficient, but not necessary, for convergence. Inserting these approximations into $\mathcal{M}\dot{\boldsymbol{U}} = \boldsymbol{F}(\boldsymbol{U})$ leads to

$$\boldsymbol{U}^{L+1,K} \approx \underbrace{\frac{\Delta t}{\mathcal{M}}\Big(\phi \boldsymbol{F}(\boldsymbol{U}^{L+1})\Big)}_{\mathcal{G}(\boldsymbol{U}^{L+1,K-1})} + \underbrace{\frac{\Delta t}{\mathcal{M}}(1-\phi)\boldsymbol{F}(\boldsymbol{U}^{L}) + \boldsymbol{U}^{L}}_{\mathcal{R}}, \tag{8.8}$$

whose contraction constant is scaled by $\eta \propto \frac{\phi \Delta t}{\mathcal{M}}$. Therefore, we see that the contraction constant η is (1) directly dependent on the strength of the interaction forces, (2) inversely proportional to $\mathcal{M}$ and (3) directly proportional to $\phi\Delta t$ (at time = t). Therefore, if convergence is slow within a time step, the time-step size, which is adjustable, can be reduced by an appropriate amount to increase the rate of convergence. Decreasing the time-step size improves the convergence, however, we want to simultaneously maximize the time-step sizes to decrease overall computing time, while still meeting an error tolerance on the numerical solution's accuracy. In order to achieve this goal, we follow an approach found in Zohdi [53–56] originally developed for continuum thermo-chemical multifield problems in which one first approximates

$$\eta^{L+1,K} \approx S(\Delta t)^p \tag{8.9}$$

(S is a constant) and secondly one assumes the error within an iteration to behave according to

$$(S(\Delta t)^p)^K \varpi^{L+1,0} = \varpi^{L+1,K}, \tag{8.10}$$

$K = 1,2,\ldots$, where $\varpi^{L+1,0}$ is the initial norm of the iterative error and S is intrinsic to the system.[11] Our goal is to meet an error tolerance in exactly a preset number of iterations. To this end, one writes

$$\left(S(\Delta t_{\text{tol}})^p\right)^{K_d} \varpi^{L+1,0} = C_{tol}, \tag{8.11}$$

where C_{tol} is a (coupling) tolerance and where K_d is the number of desired iterations.[12] If the error tolerance is not met in the desired number of iterations, the contraction constant $\eta^{L+1,K}$ is too large. Accordingly, one can solve for a new smaller step size, under the assumption that S is constant,

$$\Delta t_{\text{tol}} = \Delta t \left(\frac{\left(\frac{C_{tol}}{\varpi^{L+1,0}}\right)^{\frac{1}{pK_d}}}{\left(\frac{\varpi^{L+1,K}}{\varpi^{L+1,0}}\right)^{\frac{1}{pK}}} \right). \tag{8.12}$$

The assumption that S is constant is not critical, since the time steps are to be recursively refined and unrefined throughout the simulation. Clearly, the expression in Eq. (8.12) can also be used for time-step enlargement, if convergence is met in less than K_d iterations.[13]

Appendix B. An example of staggering-scheme/time-step convergence

For the class of coupled systems considered in this work the coupled operator's spectral radius (largest eigenvalue) controls the convergence (within a time step) of this type of method, and is directly dependent on the time-step discretization size, Δt. We consider a simple example which illustrates the essential concepts. Accordingly, consider the coupling of two first-order (ordinary differential equations) equations

$$\boxed{\begin{array}{l} a\dot{U}_1 + cU_2 = F_1, \\ b\dot{U}_2 + dU_1 = F_2. \end{array}} \tag{9.1}$$

When discretized in time, for example with a trapeziodal ϕ-method ($0 \leqslant \phi \leqslant 1$) scheme, we obtain

$$\boxed{\begin{array}{l} U_1^{L+1} = U_1^L + \frac{\Delta t}{a}\left(\phi\left(F_1^{L+1} - cU_2^{L+1}\right) + (1-\phi)\left(F_1^L - U_2^L\right)\right), \\ U_2^{L+1} = U_2^L + \frac{\Delta t}{b}\left(\phi\left(F_2^{L+1} - dU_1^{L+1}\right) + (1-\phi)\left(F_2^L - U_1^L\right)\right) \end{array}} \tag{9.2}$$

which leads to the following coupled system:

$$\begin{bmatrix} 1 & \frac{\phi\Delta t c}{a} \\ \frac{\phi\Delta t d}{b} & 1 \end{bmatrix} \begin{Bmatrix} U_1^{L+1} \\ U_2^{L+1} \end{Bmatrix} = \left\{ \begin{array}{l} \underbrace{U_1^L + \frac{\Delta t}{a}\left(\phi F_1^{L+1} + (1-\phi)\left(F_1^L - cU_2^L\right)\right)}_{\stackrel{\text{def}}{=} \gamma_1} \\ \underbrace{U_2^L + \frac{\Delta t}{b}\left(\phi F_2^{L+1} + (1-\phi)\left(F_2^L - dU_1^L\right)\right)}_{\stackrel{\text{def}}{=} \gamma_2} \end{array} \right\}. \tag{9.3}$$

Considering a recursive staggering scheme of Jacobi-type, where the updates are made only after one complete iteration, considered here only for algebraic simplicity, one has the following split[14]

$$\begin{bmatrix} 0 & \frac{\phi\Delta t c}{a} \\ \frac{\phi\Delta t d}{b} & 0 \end{bmatrix} \begin{Bmatrix} U_1^{L+1} \\ U_2^{L+1} \end{Bmatrix} + \begin{bmatrix} 1 & 0 \\ 0 & 1 \end{bmatrix} \begin{Bmatrix} U_1^{L+1} \\ U_2^{L+1} \end{Bmatrix} = \begin{Bmatrix} \gamma_1 \\ \gamma_2 \end{Bmatrix} \tag{9.4}$$

and rearranging for iterative solution

$$\underbrace{-\begin{bmatrix} 0 & \frac{\phi\Delta t c}{a} \\ \frac{\phi\Delta t d}{b} & 0 \end{bmatrix} \begin{Bmatrix} U_1^{L+1,K} \\ U_2^{L+1,K} \end{Bmatrix}}_{G(\boldsymbol{U}^{L+1,K})} + \underbrace{\begin{Bmatrix} \gamma_1 \\ \gamma_2 \end{Bmatrix}}_{\mathcal{R}} = \underbrace{\begin{Bmatrix} U_1^{L+1} \\ U_2^{L+1} \end{Bmatrix}}_{\boldsymbol{U}^{L+1,K}} \tag{9.5}$$

The eigenvalues of $\mathcal{G}$ are

$$\lambda_{1,2} = \pm\sqrt{\frac{(\phi\Delta t)^2 cd}{ab}}. \tag{9.6}$$

One sees that the convergence of the staggering scheme is directly related (linearly in this case) to the size of the time step by setting $|\lambda_{1,2}| < 1$, we obtain

$$\Delta t < \frac{1}{\phi}\sqrt{\frac{ab}{cd}}. \tag{9.7}$$

[11] For the class of problems under consideration, due to the linear dependency on Δt, $p \approx 1$.

[12] Typically, K_d is chosen to be between five to 10 iterations.

[13] At the implementation level, since the exact solution is unknown, the following relative error term is used, $\varpi^{L+1,K} \stackrel{\text{def}}{=} \boldsymbol{U}^{L+1,K} - \boldsymbol{U}^{L+1,K-1}$.

[14] A Gauss–Seidel-type approach would involve using the most current iterate. Typically, under very general conditions, if the Jacobi method converges, the Gauss–Seidel method converges at a faster rate, while if the Jacobi method diverges, the Gauss–Seidel method diverges at a faster rate. For example, see Ames [4] for details. The Jacobi method is easier to address theoretically, thus it is used for proof of convergence, and the Gauss–Seidel method at the implementation level.

Clearly, the number of iterations increase with ϕ; the least number of iterations (zero) being when an explicit Euler method is used, and the largest number of iterations being when an implicit Euler method ($\phi = 1$) is used. As pointed out in Zohdi [53], the time step induced restriction for convergence matches the radius of analyticity of a Taylor series expansion of the solution around time t.

Remark. The term $\sqrt{\frac{cd}{ab}}$ appears in the exact solution which contains exponentials of the form $Ae^{\sqrt{\frac{cd}{ab}}t}$ that dictate the rate of growth of the solution. Thus, the time step dictated by Eq. (9.7) must be small enough to "compensate" for this growth.

Appendix C. Spatial finite difference stencils

The following approximations are used (Fig. 19):

- For the first derivative of a primal variable u at (x_1, x_2, x_3):

$$\frac{\partial u}{\partial x_1} \approx \frac{u(x_1+\Delta x_1, x_2, x_3) - u(x_1-\Delta x_1, x_2, x_3)}{2\Delta x_1}. \tag{10.1}$$

- For the derivative of a flux at (x_1, x_2, x_3):

$$\begin{aligned}\frac{\partial}{\partial x_1}\left(A\frac{\partial u}{\partial x_1}\right) &\approx \frac{\left(A\frac{\partial u}{\partial x_1}\right)\Big|_{x_1+\frac{\Delta x_1}{2}, x_2, x_3} - \left(A\frac{\partial u}{\partial x_1}\right)\Big|_{x_1-\frac{\Delta x_1}{2}, x_2, x_3}}{\Delta x_1}\\ &= \frac{1}{\Delta x_1}\left(A\left(x_1+\frac{\Delta x_1}{2}, x_2, x_3\right)\right.\\ &\quad\times\left(\frac{u(x_1+\Delta x_1), x_2, x_3 - u(x_1, x_2, x_3)}{\Delta x_1}\right)\\ &\quad -A\left(x_1-\frac{\Delta x_1}{2}, x_2, x_3\right)\\ &\quad\left.\times\left(\frac{u(x_1, x_2, x_3) - u(x_1-\Delta x_1, x_2, x_3)}{\Delta x_1}\right)\right).\end{aligned} \tag{10.2}$$

- For the cross-derivative of a flux at (x_1, x_2):

$$\begin{aligned}\frac{\partial}{\partial x_2}\left(A\frac{\partial u}{\partial x_1}\right) &\approx \frac{\partial}{\partial x_2}\left(A(x_1, x_2, x_3)\left(\frac{u(x_1+\Delta x_1, x_2, x_3) - u(x_1-\Delta x_1, x_2, x_3)}{2\Delta x_1}\right)\right)\\ &\approx \frac{1}{4\Delta x_1 \Delta x_2}(A(x_1, x_2+\Delta x_2, x_3)(u(x_1+\Delta x_1, x_2+\Delta x_2, x_3)\\ &\quad - u(x_1-\Delta x_1, x_2+\Delta x_2, x_3)) - A(x_1, x_2-\Delta x_2, x_3)\\ &\quad\times(u(x_1+\Delta x_1, x_2-\Delta x_2, x_3) - u(x_1-\Delta x_1, x_2-\Delta x_2, x_3))),\end{aligned} \tag{10.3}$$

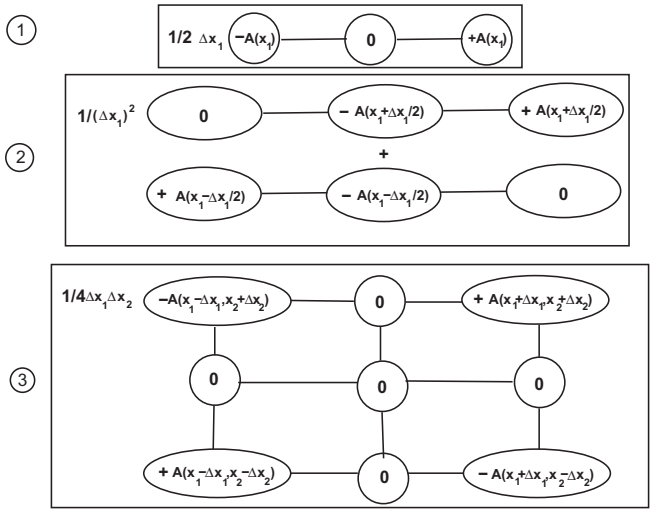

Fig. 19. The various stencils in "computational molecule" form (centered at (x, y, z)), where: (1) $\frac{\partial u}{\partial x}$, (2) $\frac{\partial}{\partial x}\left(A\frac{\partial u}{\partial x}\right)$ and (3) $\frac{\partial}{\partial y}\left(A\frac{\partial u}{\partial x}\right)$.

where

$$A\left(x_1+\frac{\Delta x_1}{2}, x_2, x_3\right) \approx \frac{1}{2}(A(x_1+\Delta x_1, x_2, x_3) + A(x_1, x_2, x_3)) \tag{10.4}$$

and

$$A\left(x_1-\frac{\Delta x_1}{2}, x_2, x_3\right) \approx \frac{1}{2}(A(x_1, x_2, x_3) + A(x_1-\Delta x_1, x_2, x_3)). \tag{10.5}$$

Appendix D. Temporally-second-order equations

D.1. Second-order equations

In order to clearly explain the time-stepping scheme, we first start with the dynamics of a particle. The equation of motion is given by

$$m\dot{\boldsymbol{v}} = \boldsymbol{\Psi}, \tag{11.1}$$

where $\boldsymbol{\Psi}$ is the total force provided from interactions with the external environment. Expanding the velocity in a Taylor series about $t + \phi\Delta t$ we obtain

$$\begin{aligned}\boldsymbol{v}(t+\Delta t) &= \boldsymbol{v}(t+\phi\Delta t) + \left.\frac{d\boldsymbol{v}}{dt}\right|_{t+\phi\Delta t}(1-\phi)\Delta t\\ &\quad + \frac{1}{2}\left.\frac{d^2\boldsymbol{v}}{dt^2}\right|_{t+\phi\Delta t}(1-\phi)^2(\Delta t)^2 + \mathcal{O}(\Delta t)^3\end{aligned} \tag{11.2}$$

and

$$\boldsymbol{v}(t) = \boldsymbol{v}(t+\phi\Delta t) - \left.\frac{d\boldsymbol{v}}{dt}\right|_{t+\phi\Delta t}\phi\Delta t + \frac{1}{2}\left.\frac{d^2\boldsymbol{v}}{dt^2}\right|_{t+\phi\Delta t}\phi^2(\Delta t)^2 + \mathcal{O}(\Delta t)^3. \tag{11.3}$$

Subtracting the two expressions yields

$$\left.\frac{d\boldsymbol{v}}{dt}\right|_{t+\phi\Delta t} = \frac{\boldsymbol{v}(t+\Delta t) - \boldsymbol{v}(t)}{\Delta t} + \hat{\mathcal{O}}(\Delta t), \tag{11.4}$$

where $\hat{\mathcal{O}}(\Delta t) = \mathcal{O}(\Delta t)^2$, when $\phi = \frac{1}{2}$. Thus, inserting this into the equations of equilibrium yields

$$\boldsymbol{v}(t+\Delta t) = \boldsymbol{v}(t) + \frac{\Delta t}{m}\boldsymbol{\Psi}(t+\phi\Delta t) + \hat{\mathcal{O}}(\Delta t)^2. \tag{11.5}$$

Note that adding a weighted sum of Eqs. (11.2) and (11.3) yields

$$\boldsymbol{v}(t+\phi\Delta t) = \phi\boldsymbol{v}(t+\Delta t) + (1-\phi)\boldsymbol{v}(t) + \mathcal{O}(\Delta t)^2, \tag{11.6}$$

which will be useful shortly. Now expanding the position of the center of mass in a Taylor series about $t + \phi\Delta t$ we obtain

$$\begin{aligned}\boldsymbol{u}(t+\Delta t) &= \boldsymbol{u}(t+\phi\Delta t) + \left.\frac{d\boldsymbol{u}}{dt}\right|_{t+\phi\Delta t}(1-\phi)\Delta t\\ &\quad + \frac{1}{2}\left.\frac{d^2\boldsymbol{u}}{dt^2}\right|_{t+\phi\Delta t}(1-\phi)^2(\Delta t)^2 + \mathcal{O}(\Delta t)^3\end{aligned} \tag{11.7}$$

and

$$\boldsymbol{u}(t) = \boldsymbol{u}(t+\phi\Delta t) - \left.\frac{d\boldsymbol{u}}{dt}\right|_{t+\phi\Delta t}\phi\Delta t + \frac{1}{2}\left.\frac{d^2\boldsymbol{u}}{dt^2}\right|_{t+\phi\Delta t}\phi^2(\Delta t)^2 + \mathcal{O}(\Delta t)^3. \tag{11.8}$$

Subtracting the two expressions yields

$$\frac{\boldsymbol{u}(t+\Delta t) - \boldsymbol{u}(t)}{\Delta t} = \boldsymbol{v}(t+\phi\Delta t) + \hat{\mathcal{O}}(\Delta t). \tag{11.9}$$

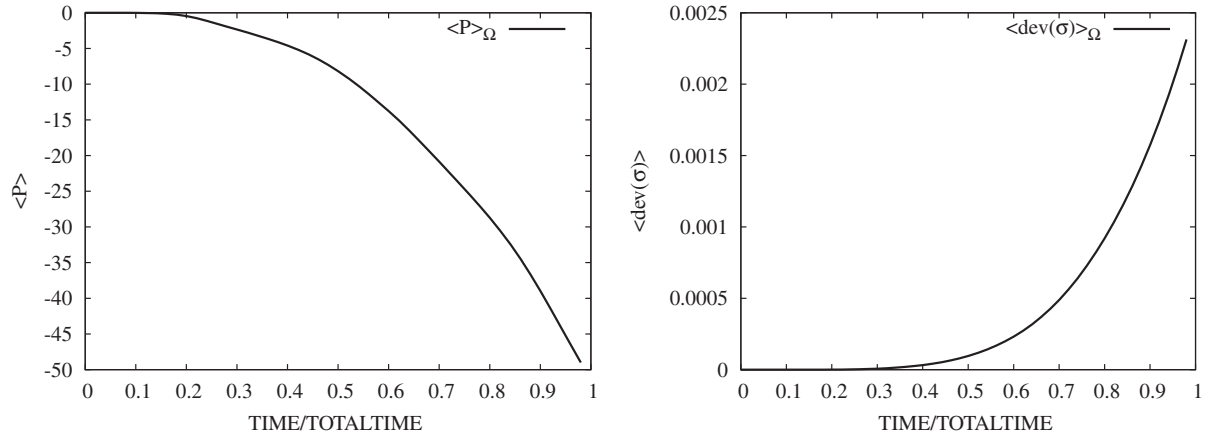

Fig. 20. Left: The volume averaged pressure $\langle \boldsymbol{p} \rangle_{\Omega}$. Right: The volume averaged normed deviator $\langle \|\boldsymbol{\sigma}'\| \rangle_{\Omega}$.

Inserting Eq. (11.6) yields

$$\boldsymbol{u}(t+\Delta t) = \boldsymbol{u}(t) + (\phi \boldsymbol{v}(t+\Delta t) + (1-\phi)\boldsymbol{v}(t))\Delta t + \hat{\mathcal{O}}(\Delta t)^2 \quad (11.10)$$

and thus using Eq. (11.5) yields

$$\boldsymbol{u}(t+\Delta t) = \boldsymbol{u}(t) + \boldsymbol{v}(t)\Delta t + \frac{\phi(\Delta t)^2}{m}\boldsymbol{\Psi}(t+\phi\Delta t) + \hat{\mathcal{O}}(\Delta t)^2. \quad (11.11)$$

The term $\boldsymbol{\Psi}(t+\phi\Delta t)$ can be handled in two main ways:

- $\boldsymbol{\Psi}(t+\phi\Delta t) \approx \boldsymbol{\Psi}(\phi \boldsymbol{u}(t+\Delta t) + (1-\phi)\boldsymbol{u}(t))$ or
- $\boldsymbol{\Psi}(t+\phi\Delta t) \approx \phi\boldsymbol{\Psi}(\boldsymbol{u}(t+\Delta t)) + (1-\phi)\boldsymbol{\Psi}(\boldsymbol{u}(t))$.

The differences are quite minute between either of the above, thus, for brevity, we choose the latter. In summary, we have the following:

$$\boldsymbol{u}(t+\Delta t) = \boldsymbol{u}(t) + \boldsymbol{v}(t)\Delta t + \frac{\phi(\Delta t)^2}{m}(\phi\boldsymbol{\Psi}(\boldsymbol{u}(t+\Delta t)) + (1-\phi)\boldsymbol{\Psi}(\boldsymbol{u}(t))) + \hat{\mathcal{O}}(\Delta t)^2. \quad (11.12)$$

We note that

- When $\phi = 1$, then this is the (implicit) Backward Euler scheme, which is very stable (very dissipative) and $\mathcal{O}(\Delta t)^2$ locally in time.
- When $\phi = 0$, then this is the (explicit) Forward Euler scheme, which is conditionally stable and $\mathcal{O}(\Delta t)^2$ locally in time.
- When $\phi = 0.5$, then this is the (implicit) "Midpoint" scheme, which is stable and $\hat{\mathcal{O}}(\Delta t)^2 = \mathcal{O}(\Delta t)^3$ locally in time.

In summary, we have for the velocity[15]

$$\boldsymbol{v}(t+\Delta t) = \boldsymbol{v}(t) + \frac{\Delta t}{m}(\phi\boldsymbol{\Psi}(t+\Delta t) + (1-\phi)\boldsymbol{\Psi}(t)) \quad (11.13)$$

and for the position

$$\begin{aligned}\boldsymbol{u}(t+\Delta t) &= \boldsymbol{u}(t) + \boldsymbol{v}(t+\phi\Delta t)\Delta t \\ &= \boldsymbol{u}(t) + (\phi\boldsymbol{v}(t+\Delta t) + (1-\phi)\boldsymbol{v}(t))\Delta t, \end{aligned} \quad (11.14)$$

or more explicitly

$$\boldsymbol{u}(t+\Delta t) = \boldsymbol{u}(t) + \boldsymbol{v}(t)\Delta t + \frac{\phi(\Delta t)^2}{m}(\phi\boldsymbol{\Psi}(t+\Delta t) + (1-\phi)\boldsymbol{\Psi}(t)). \quad (11.15)$$

[15] In order to streamline the notation, we drop the cumbersome $\mathcal{O}(\Delta t)$-type terms.

In the continuum formulation, $\nabla_x \cdot \boldsymbol{T} + \boldsymbol{f} = \rho\ddot{\boldsymbol{u}}, m = \rho$ and $\boldsymbol{\Psi} = \nabla_x \cdot \boldsymbol{T} + \boldsymbol{f}$ where we must apply the (iterative) process introduced earlier to each node in the system. Under infinitesimal deformations, $\nabla_X \cdot \boldsymbol{T} + \boldsymbol{f} = \rho_o \frac{\partial^2 \boldsymbol{u}}{\partial t^2}, m = \rho_o$ and $\boldsymbol{\Psi} = \nabla_X \cdot \boldsymbol{T} + \boldsymbol{f}$.

Appendix E. An electro–magneto–thermo–mechano–chemo numerical example

As an example, in addition to the previous electromagnetic, the following parameters were used (see the equations in the main body of the paper for variable definitions)[16]:

- The displacement boundary condition: $\boldsymbol{u}|_{\partial\Omega} = \boldsymbol{0}$.
- The (interior) displacement initial condition: $\boldsymbol{u}(x_1, x_2, x_3) = \boldsymbol{0}$.
- The chemical concentration boundary condition: $c|_{\partial\Omega} = 1000$.
- The (interior) chemical concentration initial condition: $c(x_1, x_2, x_3) = 0$.
- The matrix material shear modulus $\mu_m^{sh} = 50$ GPa.
- The particle material shear modulus $\mu_p^{sh} = 100$ GPa.
- The matrix material Lame parameter $\lambda_m = 100$ GPa.
- The particle material Lame parameter $\lambda_p = 200$ GPa.
- The matrix material thermal expansion coefficient $\beta_m = 10^{-6}$.
- The particle material thermal expansion coefficient $\beta_p = 5 \times 10^{-6}$.
- The matrix material chemical heat generation parameter (for the First Law of Thermodynamics) $\eta_m = 1000$; recall $\rho_o z = \eta|\dot{c}|$.
- The particle material chemical heat generation parameter $\eta_p = 5000$.
- The matrix material chemical damage rate parameter $a_{1m} = -10$.
- The particle material chemical damage rate parameter $a_{1p} = -50$.
- The matrix material pressure damage rate parameter $a_{2m} = -10$.
- The particle material pressure damage rate parameter $a_{2p} = -50$.
- The matrix material deviatoric damage rate parameter $a_{3m} = -10$.
- The particle material deviatoric damage rate parameter $a_{3p} = -50$.
- The matrix material critical pressure parameter $k_{1m} = 10$ MPa.
- The particle material critical pressure parameter $k_{1p} = 50$ MPa.
- The matrix material critical deviatoric norm parameter $k_{2m} = 10$ MPa.

[16] The thermally-sensitive case was considered here. Also, the matrix material was signified with a subscript "m" and the particle material with a subscript "p" for clarity.

- The particle material critical deviatoric norm $k_{2p} = 50$ MPa.
- The matrix material first reaction rate parameter $r_{1m} = 10^{-6}$.
- The particle material reaction rate parameter $r_{1p} = 5 \times 10^{-6}$.
- The matrix material reaction rate parameter $r_{2m} = 10^{-6}$.
- The particle material reaction rate parameter $r_{2p} = 5 \times 10^{-6}$.
- The matrix material baseline diffusivity $D_m = 1$.
- The particle material baseline diffusivity $D_p = 5$.
- The matrix material activation energy parameters for the reaction rate (r_{1m}): $Q_{11m} = 100$, $Q_{12m} = 10^{-6}$ for the following $\tau_1 = r_1 e^{\frac{Q_{11} - Q_{12p}}{R\theta}}$.
- The particle material activation energy parameters for the reaction rate (r_{1p}): $Q_{11p} = 500$, $Q_{12p} = 5 \times 10^{-6}$.
- The matrix material activation energy parameters for the reaction rate (r_{2m}): $Q_{21m} = 100$, $Q_{22m} = 10^{-6}$ for the following $\tau_2 = r_2 e^{\frac{Q_{21} - Q_{22p}}{R\theta}}$.
- The particle material activation energy parameters for the reaction rate (r_{2p}): $Q_{21p} = 500$, $Q_{22p} = 5 \times 10^{-6}$.
- The matrix material activation energy parameters for the diffusion (D_{om}): $U_{11m} = 100$, $U_{12m} = 10^{-6}$ for the following $\mathbb{D} = \mathbb{D}_o e^{\frac{U_{21} - U_{22p}}{R\theta}}$.
- The particle material activation energy parameters for the reaction rate (D_{op}): $U_{21p} = 500$. $U_{22p} = 5 \times 10^{-6}$.

The results are shown in Figs. 20–23.

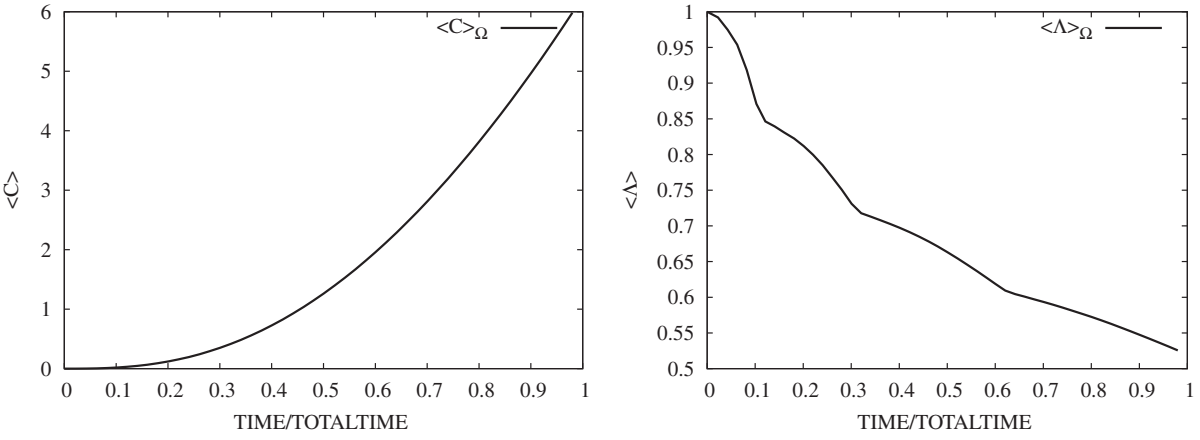

Fig. 21. Left: The volume averaged concentration $\langle c \rangle_\Omega$. Right: The volume averaged damage indicator $\langle \Lambda \rangle_\Omega$.

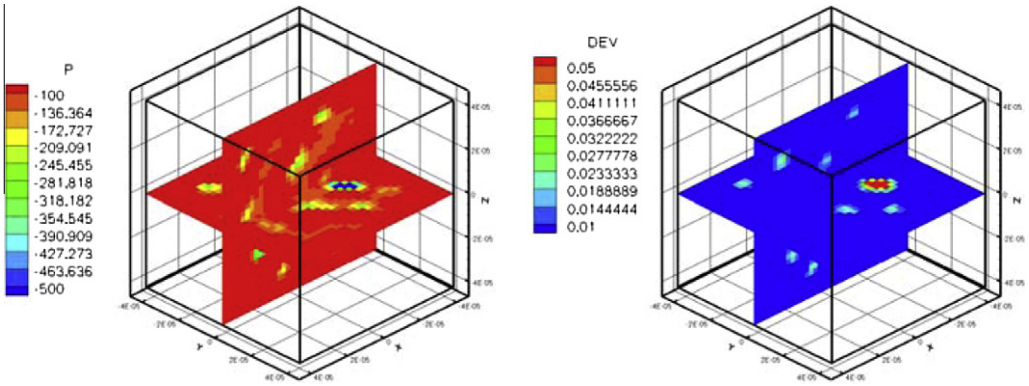

Fig. 22. Internal probe: Left: The pressure $\boldsymbol{p}$. Right: The normed deviator $\|\boldsymbol{\sigma}'\|$ (in megapascals).

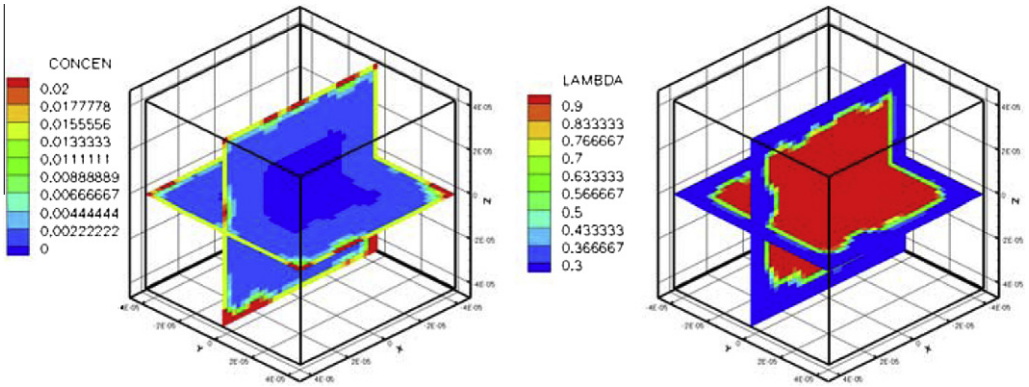

Fig. 23. Internal probe: Left: The chemical concentration $\boldsymbol{c}$. Right: The damage indicator Λ.

References

[1] J. Aboudi, Mechanics of Composite Materials – A Unified Micromechanical Approach, Elsevier, 1992. p. 29.
[2] G. Amdahl, The validity of a single processor approach to achieving large-scale computing capabilities, in: Proceedings of AFIPS Spring Joint Computer Conference, AFIPS Press, 1967, pp. 483–485.
[3] O. Axelsson, Iterative Solution Methods, Cambridge University Press, 1994.
[4] W.F. Ames, Numerical Methods for Partial Differential Equations, second ed., Academic Press, 1977.
[5] M. Bianco, G. Bilardi, F. Pesavento, G. Pucci, B.A. Schrefler, A frontal solver tuned for fully coupled non-linear hygro-thermo-mechanical problems, Int. J. Numer. Methods Engrg. 57 (2003) 1801–1818.
[6] J. Crank, The Mathematics of Diffusion, second ed., Oxford Science Publications, 1975.
[7] L. Demkowicz, Computing with hp-Adaptive Finite Elements. I. One- and Two-dimensional Elliptic and Maxwell Problems, CRC Press, Taylor and Francis, 2006.
[8] L. Demkowicz, J. Kurtz, D. Pardo, M. Paszynski, W. Rachowicz, A. Zdunek, Computing with Hp-Adaptive Finite Elements, Frontiers: Three Dimensional Elliptic and Maxwell Problems with Applications, vol. 2, CRC Press, Taylor and Francis, 2007.
[9] A. Donev, I. Cisse, D. Sachs, E.A. Variano, F. Stillinger, R. Connelly, S. Torquato, P. Chaikin, Improving the density of jammed disordered packings using ellipsoids, Science 303 (2004) 990–993.
[10] A. Donev, S. Torquato, F. Stillinger, Neighbor list collision-driven molecular dynamics simulation for nonspherical hard particles – I. Algorithmic details, J. Comput. Phys. 202 (2005) 737.
[11] A. Donev, S. Torquato, F. Stillinger, Neighbor list collision-driven molecular dynamics simulation for nonspherical hard particles – II. Application to ellipses & ellipsoids, J. Comput. Phys. 202 (2005) 765.
[12] C.P. Flynn, Point Defects and Diffusion, Clarendon Press, Oxford, 1972.
[13] J.L. Gustafson, Reevaluating Amdahl's law, Commun. ACM 31 (5) (1988) 532–533.
[14] Z. Hashin, S. Shtrikman, On some variational principles in anisotropic and nonhomogeneous elasticity, J. Mech. Phys. Solids 10 (1962) 335–342.
[15] Z. Hashin, S. Shtrikman, A variational approach to the theory of the elastic behaviour of multiphase materials, J. Mech. Phys. Solids 11 (1963) 127–140.
[16] Z. Hashin, Analysis of composite materials: a survey, ASME J. Appl. Mech. 50 (1983) 481–505.
[17] Z. Hashin, S. Shtrikman, A variational approach to the theory of effective magnetic permeability of multiphase materials, J. Appl. Phys. 33 (10) (1962) 3125–3131.
[18] J.D. Jackson, Classical Electrodynamics, third ed., Wiley, 1998.
[19] V.V. Jikov, S.M. Kozlov, O.A. Olenik, Homogenization of Differential Operators and Integral Functionals, Springer-Verlag, 1994.
[20] L.M. Kachanov, Introduction to Continuum Damage Mechanics, Martinus Nijoff, Dordricht, 1986.
[21] A. Kansaal, S. Torquato, F. Stillinger, Diversity of order & densities in jammed hard-particle packings, Phys. Rev. E 66 (2002) 041109.
[22] K.S. Kunz, R.J. Luebbers, The Finite Difference Time Domain Method for Electromagnetics, CRC Press, 1993.
[23] R.W. Lewis, B.A. Schrefler, L. Simoni, Coupling versus uncoupling in soil consolidation, Int. J. Numer. Anal. Methods Geomech. 15 (1992) 533–548.
[24] R.W. Lewis, B.A. Schrefler, The Finite Element Method in the Static and Dynamic Deformation and Consolidation of Porous Media, second ed., Wiley Press, 1998.
[25] X. Markenscoff, Diffusion induced instability, Quart. Appl. Mech. LIX (1) (2001) 147–151.
[26] X. Markenscoff, Instabilities of a thermo-mechano-chemical system, Quart. Appl. Mech. LIX (3) (2001) 471–477.
[27] X. Markenscoff, On conditions of "negative creep" in amorphous solids, Mech. Mater. 35 (3-6) (2003) 553–557.
[28] J.C. Maxwell, On the dynamical theory of gases, Philos. Trans. Soc. London 157 (1867) 49.
[29] J.C. Maxwell, A Treatise on Electricity and Magnetism, third ed., Clarendon Press, Oxford, 1873.
[30] T. Mura, Micromechanics of defects in solids, second ed., Kluwer Academic Publishers, 1993.
[31] S. Nemat-Nasser, M. Hori, Micromechanics: Overall Properties of Heterogeneous Solids, second ed., Elsevier, Amsterdam, 1999.
[32] M. Papadrakakis, Solving Large-Scale Problems in Mechanics, John Wiley and Sons, 1993.
[33] M. Papadrakakis, Parallel Solution Methods in Computational Mechanics, John Wiley and Sons, 1997.
[34] M. Papadrakakis, N.D. Lagaros, Y. Fragakis, Parallel computational strategies for structural optimisation, Int. J. Numer. Methods Engrg. (2003).
[35] W. Rachowicz, A. Zdunek, Automated multi-level substructuring (AMLS) for electromagnetics, Comput. Methods Appl. Mech. Engrg. 198 (13–14) (2009) 1224–1234.
[36] J.W. Rayleigh, On the influence of obstacles arranged in rectangular order upon properties of a medium, Philos. Mag. 32 (1892) 481–491.
[37] B.A. Schrefler, A partitioned solution procedure for geothermal reservoir analysis, Commun. Appl. Numer. Methods 1 (1985) 53–56.
[38] G.M. Stavroulakis, M. Papadrakakis, Advances on the domain decomposition solution of large scale porous media problems, Comput. Methods Appl. Mech. Engrg. 198/21–26 (2009) 1935–1945.
[39] A. Taflove, S. Hagness, Computational Electrodynamics: The Finite-Difference Time-Domain Method, third ed., Artech Press, 2005.
[40] S. Torquato, Random Heterogeneous Materials: Microstructure and Macroscopic Properties, Springer-Verlag, New York, 2001.
[41] E. Turska, B.A. Schrefler, On consistency, stability and convergence of staggered solution procedures, Rend. Mat. Acc. Lincei, Rome 5 (9) (1994) 265–271.
[42] X. Wang, B.A. Schrefler, A multifrontal parallel algorithm for coupled thermo-hydro-mechanical analysis of deforming porous media, Int. J. Numer. Methods Eng. 43 (1998) 10691083.
[43] B. Widom, Random sequential addition of hard spheres to a volume, J. Chem. Phys. 44 (1966) 3888–3894.
[44] O. Wiener, Zur Theorie der Refraktionskonstanten. Berichte über die Verhandlungen der Königlich-Sächsischen Gesellschaft der Wissenshaften zu Leipzig, vol. Math.-phys Klasses, Band 62, pp. 256–277, 1910.
[45] K. Yee, Numerical solution of initial boundary value problems involving Maxwell's equations in isotropic media, IEEE Trans. Antennas Propagat. 14 (1966) 302.
[46] D.M. Young, Iterative Methods for Solving Partial Difference Equations of Elliptic Type, Doctoral Thesis, Harvard University, 1950
[47] O.C. Zienkiewicz, Coupled problems & their numerical solution, in: R.W. Lewis, P. Bettes, E. Hinton (Eds.), Numerical Methods in Coupled Systems, Wiley, Chichester, 1984, pp. 35–58.
[48] O.C. Zienkiewicz, D.K. Paul, A.H.C. Chan, Unconditionally stable staggered solution procedure for soil-pore fluid interaction problems, Int. J. Numer. Methods Engrg. 26 (1988) 1039–1055.
[49] T.I. Zohdi, P. Wriggers, A domain decomposition method for bodies with microstructure based upon material regularization, Int. J. Solids Struct. 36 (17) (1999) 2507–2526.
[50] T.I. Zohdi, P. Wriggers, Aspects of the computational testing of the mechanical properties of microheterogeneous material samples, Int. J. Numer. Methods Engrg. 50 (2001) 2573–2599.
[51] T.I. Zohdi, P. Wriggers, Computational micro–macro material testing, Arch. Comput. Methods Engrg. 8 (2) (2001) 131–228.
[52] T.I. Zohdi, P. Wriggers, C. Huet, A method of substructuring large-scale computational micromechanical problems, Comput. Methods Appl. Mech. Engrg. 190 (43–44) (2001) 5639–5656.
[53] T.I. Zohdi, An adaptive-recursive staggering strategy for simulating multifield coupled processes in microheterogeneous solids, Int. J. Numer. Methods Engrg. 53 (2002) 1511–1532.
[54] T.I. Zohdi, Modeling and simulation of a class of coupled thermo-chemo-mechanical processes in multiphase solids, Comput. Methods Appl. Mech. Engrg. 193/6–8 (2004) 679–699.
[55] T.I. Zohdi, On the computation of the coupled thermo-electromagnetic response of continua with particulate microstructure, Int. J. Numer. Methods Engrg. 76 (2008) 1250–1279.
[56] T.I. Zohdi, P. Wriggers, Introduction to Computational Micromechanics, Springer-Verlag, 2008. Second Reprinting.
[57] T.I. Zohdi, Simulation of time-discontinuous chemically-aided intergranular fracture, Comput. Mater. Sci. 24 (4) (2002) 490–500.
[58] T.I. Zohdi, K. Hutter, P. Wriggers, A technique to describe the macroscopic pressure dependence of diffusive properties of solid materials containing heterogeneities, Comput. Mater. Sci. 15 (1999) 69–88.
[59] T.I. Zohdi, Some remarks on hydrogen trapping, Int. J. Fract. 106 (2) (2000) L9–L14.